WIND VARIABILITY OF B SUPERGIANTS. I. THE RAPID ROTATOR HD 64760 (B0.5 Ib)

DERCK MASSA[1]

Applied Research Corporation, 8201 Corporate Drive, Landover, MD 20786; massa@godot.arclch.com

RAMAN K. PRINJA

Department of Physics and Astronomy, University College London, Gower Street, London WC1E 6BT, UK; rkp@starlink.ucl.ac.uk

AND

ALEXANDER W. FULLERTON[2,3]

Bartol Research Institute, University of Delaware, Newark, DE 19716-4793; alex@usm.uni-muenchen.de

ABSTRACT

We present the results of a 6 day time series of observations of the rapidly rotating B0.5 Ib star HD 64760. We point out several reasons why such intermediate luminosity B supergiants are ideal targets for wind variability studies and then present our results that show the following: (1) continuous wind activity throughout the 6 day run with the wind never in steady state for more than a few hr; (2) wind variability very near $v = 0$ km s^{-1} in the resonance lines from the lower ionization stages (Al III and C II); (3) a distinct correlation between variability in the Si III $\lambda\lambda1300$ triplets, the strong C III $\lambda1247$ singlet, and the onset of extremely strong wind activity, suggesting a connection between photospheric and wind activity; (4) long temporal coherence in the behavior of the strong absorption events; (5) evidence for large-scale spatial coherence, implied by a whole scale, simultaneous weakening in the wind absorption over a wide range in velocities; (6) ionization variability in the wind accompanying the largest changes in the absorption strengths of the wind lines.

In addition, modeling of the wind lines provides the following information about the state the wind in HD 64760. (1) The number of structures on the portion of a constant velocity surface occulting the stellar disk at a particular time must be quite small, while the number on the entire constant velocity surface throughout the wind must be large. (2) The escape probability at low velocity is overestimated by a normal $\beta \sim 1$ velocity law, perhaps due to the presence of low-velocity shocks deep in the wind or a shallow velocity gradient at low velocity. (3) Estimates of the ionization structure in the wind indicate that the ionization ratios are not those expected from thermal equilibrium wind models or from an extrapolation of previous O star results. The large observed $q(\text{N v})/q(\text{Si iv})$ ratio is almost certainly due to distributed X-rays, but the level of ionization predicted by distributed X-ray wind models is inconsistent with the predicted mass-loss rate. Thus, it is impossible to reconcile the observed ionization ratios and the predicted mass-loss rate within the framework of the available models.

Subject headings: stars: activity — stars: early-type — stars: individual (HD 64760) — stars: mass loss — ultraviolet: stars

1. INTRODUCTION

Wind activity in the UV wind lines of luminous OB stars was first noted in repeated observations of hot stars by the *Copernicus* satellite (see, e.g., York et al. 1977; Snow 1977). However, the true nature and the details of this behavior was not even remotely understood until the advent of *IUE* (Boggess et al. 1978a, b). *IUE* observations established that wind activity is actually an entirely new class of variability in hot stars, which is ubiquitous among those objects with wind lines sufficiently well developed to reveal variability, but not so saturated as to mask it (for recent reviews, see, e.g., Moffat et al. 1995). The ubiquity of the variability implies that it is an intrinsic property of hot-star winds, and that steady state descriptions of them are, at best, ill-defined mean representations of the stellar wind flows.

Time series observations with *IUE* have demonstrated several interesting aspects of wind variability in hot stars (excluding Be stars and subdwarfs). First, in most O stars, the wind activity is usually observed as discrete absorption components (DACs), which are generally recognized as localized optical depth enhancements that appear at intermediate velocities and accelerate toward higher velocity (Henrichs 1988; Prinja 1992; Howarth 1992). Second, it has been shown that the DACs in O stars can account for as much as 50% of the wind material (Lamers, Gathier, & Snow 1982), although 10%–20% maybe more common (Prinja & Howarth 1986). Third, a strong correlation between the acceleration and recurrence of DACs and the projected rotation velocity, $v \sin i$, has been observed (Prinja 1988, 1992; Kaper 1993). The nature and origin of this connection remains unclear.

Although the mechanisms responsible for wind variability are not presently understood, the fluctuations are believed to be signatures of instabilities that disrupt the wind flow (see, e.g., Puls, Owocki, & Fullerton 1993). One theoretical picture of wind activity (Owocki 1995, Moffat & Robert 1994) suggests that the action of these instabilities fragments the wind into

numerous, small clumps that individually do not cover a very large solid angle, and whose large number may account, e.g., for the stability of the X-ray fluxes observed from OB stars. However, the DACs and related wind variability observed in the UV profiles require structure on a *much larger scale*. For example, since DACs can be quite strong at relatively low velocity, the structure responsible for them must be two-dimensional and spatially coherent over a sizable fraction of a stellar hemisphere. Numerical simulations show that such large-scale features can also form in wind flows, but that lateral coherence must be introduced through amplification (by the nonlocal radiative driving) of an explicit disturbance introduced near the wind base (see Owocki 1995).

Thus, we see that some important observational questions that need to be addressed are the following:

1. At what depth in the wind do the structures responsible for UV wind line variability form? The physical processes required to generate structure can be very different depending upon whether the structures arise deep in the supersonic wind or in the subsonic photospheric layers of the atmosphere.

2. Is there a wind-photosphere connection, i.e., is the wind variability *causally* linked to perturbations due to photospheric processes?

3. How does the ionization of the wind respond to changes in the wind density? Are the observed time-dependent changes in the ionization structure consistent with the presence of the shock phenomena predicted by theory?

Although most UV wind variability studies to date have concentrated on O and WR stars, the diagnostics available in spectra of B0–1 supergiants of intermediate luminosity (hereafter BIs) present distinct advantages for addressing these observational issues. Some of these advantages are the following:

1. BIs have well-developed but unsaturated wind lines that span a wide range of ionization stages, thereby allowing the time-dependent ionization structure of the wind to be diagnosed. These diagnostics run from C II to C IV at B1 and from Si III to N V at B0 and include adjacent stages of ionization for Si (in particular, Si III λ1206 and Si IV $\lambda\lambda$1395, 1403).

2. After hydrogen, the UV photospheric lines of BIs are the strongest features in their spectra. The UV photospheric silicon lines are sensitive temperature and surface gravity diagnostics, and the strongest of these lines also show wind effects (Massa, Shore, & Wynne 1992). Therefore, these lines serve as excellent probes of the wind-photosphere interface.

3. BIs have lower terminal speeds and larger radii than O stars, which imply that their flow times ($t_{flow} \propto R/v_\infty$ for a steady wind) are longer and their rotational periods will tend to be longer (for a given $v \sin i$); consequently, the spectroscopic signatures of their wind variability will evolve more slowly. Thus, wind variations in BIs are easier to observe, especially at low velocities where the accelerations are largest. In addition, the lower terminal velocities mean that the two components of the important Si IV $\lambda\lambda$1400 doublet become largely uncoupled.

Although " snapshot " *IUE* observations of BIs separated by months or more show distinct changes in their wind lines (see the discussion by Prinja & Howarth 1986), the few existing time series are either not long enough to follow the progression of wind features, or else show little wind activity over the duration of the series (typically 2–3 days; e.g., note the behavior of

HD 164402 in Fig. 5 of Prinja 1992). Nevertheless, on the basis of the correlation between the appearance and evolution of DACs in the winds of O type stars with $v \sin i$, we expect rapidly rotating BIs to show more frequent and more rapid wind variability. Therefore, in 1993 March we obtained a 6 day *IUE* time series of three rapidly rotating BIs. All three showed continuous wind activity, and one of them, HD 64760, is the subject of the current paper.

The remainder of this paper is organized in the following manner. Section 2 describes the observations and the reduction procedures. The photospheric and wind spectra of HD 64760 are discussed in § 3, and compared to other, more slowly rotating BIs. Section 4 presents the time series observations, beginning with a descriptive overview of the data, and includes the identification and analysis of the distinguishable DACs. Section 5 presents a detailed modeling analysis of the wind lines, and an analysis of their variability. Section 6 summarizes our main findings.

2. THE DATA

The observations consist of 56 spectra spanning 5.9 days from 1993 March 6–11. The data were obtained through the large aperture of the SWP camera in the high-dispersion mode. The exposure times were 60 s, with a mean sampling time of ~ 2.5 hr, except for two gaps (due to time allocated to an AGN monitoring campaign) of approximately 6.5 hr, which occurred at about 1 and 5 days into the program. A log of the observations is given in Table 1. We list the SWP image numbers, the decimal HJD at the beginning of each observation, the time in decimal hours from the beginning of the run, Δt, and the mean flux number, $\langle FN \rangle$, of each spectrum. The latter quantity varies considerably because of complications involved with

TABLE 1

IUE Observing Log

SWP	HJD[*]	Δt (hr)	$\langle FN \rangle$	SWP	HJD[*]	Δt (hr)	$\langle FN \rangle$
47094......	51.182	0.0	67	47179......	54.173	71.8	334
47097......	51.280	2.4	338	47182......	54.299	74.8	148
47100......	51.377	4.7	418	47185......	54.408	77.4	391
47103......	51.484	7.3	408	47188......	54.533	80.4	419
47106......	51.590	9.8	415	47191......	54.627	82.7	415
47109......	51.689	12.2	386	47194......	54.722	85.0	410
47112......	51.797	14.8	426	47197......	54.819	87.3	379
47115......	51.910	17.5	426	47200......	54.912	89.5	405
47118......	52.018	20.1	421	47203......	55.012	91.9	412
47121......	52.115	22.4	423	47206......	55.117	94.5	411
47124......	52.244	25.5	403	47209......	55.251	97.7	397
47128......	52.524	32.2	413	47212......	55.365	100.4	113
47131......	52.609	34.2	415	47215......	55.487	103.3	412
47134......	52.694	36.3	391	47218......	55.578	105.5	415
47137......	52.786	38.5	386	47221......	55.669	107.7	416
47140......	52.876	40.7	408	47224......	55.761	110.1	405
47143......	52.971	42.9	399	47227......	55.851	112.1	272
47146......	53.058	45.0	365	47230......	55.945	114.3	352
47149......	53.180	48.0	394	47233......	56.046	116.7	306
47152......	53.295	50.7	405	47236......	56.151	119.3	63
47155......	53.400	53.2	388	47239......	56.253	121.7	364
47158......	53.507	55.8	413	47243......	55.531	128.4	396
47161......	53.606	58.2	302	47246......	56.624	130.6	422
47164......	53.707	60.6	289	47249......	56.718	132.9	382
47167......	53.808	63.0	413	47252......	56.815	135.2	411
47170......	53.893	65.1	345	47255......	56.899	137.2	405
47173......	53.983	67.2	291	47258......	56.990	139.4	401
47176......	54.071	69.3	370	47261......	57.092	141.8	401

* HJD − 2,449,000.0

centering the star in the aperture in the presence of the FES "streak." The streak is scattered light on the FES field of *IUE* (see Weinstein & Carini 1992) that can, under certain circumstances, make it impossible to identify the star when it is near the aperture. Consequently, we were forced to place the image of HD 64760 near the edge of the FES field and then move the spacecraft to position the star in the aperture. Because the streak was a recent occurrence at the time of our observations, the *IUE* observatory staff had not yet fully mapped the distortions in the FES field and the star was frequently not centered in the aperture after the maneuver. This caused considerable light loss in a few cases, corrupted the photometric integrity of the data, and caused the signal-to-noise properties of the data to vary from one spectrum to the next. Nevertheless, most of the exposures were within 75% of optimal, and only 4 of the 56 spectra have very poor signal-to-noise ratios.

All the spectra were extracted in a uniform manner from the two-dimensional photometrically linearized (PHOT) images by using the IUEDR package (Giddings & Rees 1989). Some advantages of IUEDR extractions compared to those performed by the standard *IUE* project software are described by Howarth & Prinja (1989). In particular, IUEDR yields considerably more reliable results at the shortest wavelengths, providing superior data quality for the important Si III $\lambda1206$ and N V $\lambda\lambda1240$ wind lines. The individual spectra were binned onto a wavelength grid with a regular sampling interval of 0.1 Å. Finally, the individual spectra were normalized over the wavelength interval 1600–1800 Å (which is free of variable features) to compensate for exposure to exposure light losses resulting from the star being improperly centered in the aperture. The lack of short-wavelength continuum variation in the gray-scale plots discussed in § 4.1 demonstrates that no color term resulted from the light loss. In addition to the observations listed in Table 1, four images (SWP 1781, 1797, 4192 and 7718) were retrieved from the *IUE* archive and processed in the same manner for use in the analysis.

3. THE STAR

In this section, we compare the spectroscopic properties of HD 64760 (see Table 2) with other B supergiants. Because it is a rapidly rotating star, we are concerned that it may not be representative of normal, less rapidly rotating stars, or that the rotation may dominate its wind flow, as in the case for HD 93521 (see Howarth & Reid 1993; Massa 1995).

We selected a number of intermediate-luminosity B0–1 supergiants from the *IUE* archives. These served as a morphological grid for placing the UV spectrum of HD 64760 into

TABLE 2
STELLAR PARAMETERS

Parameter	Value	Reference
Spectral type	B0.5 Ib	Hoffleit & Jaschek (1982)
V	4.24	Hoffleit & Jaschek (1982)
$(B - V)$	−0.15	Hoffleit & Jaschek (1982)
$N(H\,\textsc{i})$ (cm^2)	1.4×10^{20}	This paper
$v \sin i$ (km s^{-1})	238	Hoffleit & Jaschek (1982)
v_∞ (km s^{-1})	1500	This paper
M_v (mag)	−6.0	Humphreys & McElroy (1984)
$L/L_\odot$	1.3×10^5	Humphreys & McElroy (1984)
$T_{\rm eff}$ (K)	23100	Humphreys & McElroy (1984)
$M/M_\odot$	20	Schaller et al. (1992)
$R/R_\odot$	22	Schaller et al. (1992)
T (rotation) (days)	4.9	(Upper limit)

context. The star in our archival sample that is spectroscopically most similar to HD 64760 is HD 100276 (SWP image number 22147). HD 100276 is also a B0.5 Ib but has a more typical rotation velocity ($v \sin i = 121$ km s^{-1}; Balona 1975). Furthermore, HD 100276 fits nicely into the surrounding UV spectral sequence, and seems normal in every way. The following sections compare the photospheric and wind lines of the two stars.

3.1. *The Photospheric Spectrum*

Massa (1989) discussed several silicon lines that are useful for classifying the UV spectra of B stars. Figure 1 compares selected portions of the spectra of HD 64760 and HD 100276. The spectrum of HD 100276 was "spun up" with an additional 200 km s^{-1} of rotational broadening (rotational convolutions add in quadrature) to simulate the broadening in HD 64760. No special attention was given to interstellar lines, so they were broadened along with the rest of the spectrum. Of particular importance is the fact that the ratios of the fine-structure Si II lines ($\lambda1265$ or $\lambda1309$) to the Si III $\lambda\lambda1300$ triplets are very similar in both stars, as are the ratios of their $\lambda\lambda1300$ lines to either of the Si III singlets, $\lambda1312$ or $\lambda1417$. Massa (1989) has shown that these line ratios are sensitive temperature and luminosity diagnostics, respectively. In fact, the overall appearance of the two stars is remarkably similar, implying that the photospheric conditions in HD 64760 are not strongly affected by its high rotational velocity.

3.2. *The Wind Lines*

The first thing to notice about the wind lines in the two stars shown in Figure 1 is their overall similarity. Both the extent and shapes of the profiles due to a wide range of ionization stages (Si III $\lambda1206$, Si IV $\lambda\lambda1393$, 1402, C IV $\lambda\lambda1548$, 1550, N V $\lambda\lambda1238$, 1242 and Al III $\lambda\lambda1854$, 1862—not shown) agree. Furthermore, the strong wind lines in HD 64760 are uniformly strong, all the way to the terminal velocity, indicating that the entire disk of the star is covered by a high-velocity wind. It is also important that its major wind lines are well-developed, but *unsaturated* (although C IV is approaching saturation). Thus, we conclude that the global wind structures of HD 64760 and HD 100276 are very similar, so the ionization structure and mass-loss rate of the wind in HD 64760 are not strongly affected by its rapid rotation.

3.3. *Summary*

The results of this section demonstrate that HD 64760 is, in all respects, a normal B0.5 Ib. Its photospheric and wind lines are similar to those of normal, less rapidly rotating supergiants of the same spectral and luminosity class. Hence, although the rapid rotation of the star may be causing an increase in its wind activity, it does not appear to dominate the structure of its wind. Consequently, it seems safe to assume that the wind activity we observe in HD 64760 is indicative of BIs in general and that its physical parameters are indicative of a normal B0.5 Ib (see Table 2).

4. THE TIME SERIES

4.1. *Overview*

This section presents a descriptive overview of the observational data, pointing out what we perceive as the most interesting aspects. The incidence of profile variability in HD 64760 is shown as gray-scale representations in Figure 2 for the Si III
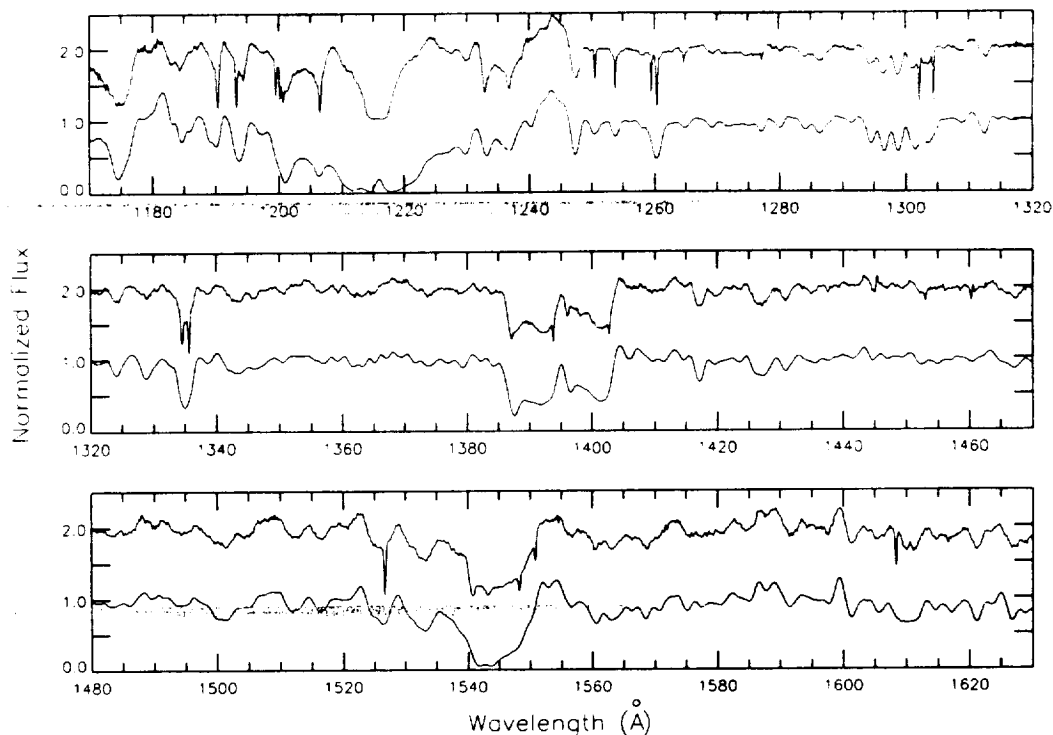
FIG. 1.—Comparison of portions of the normalized UV spectra of the two B0.5 Ib stars HD 64760 (*top*, offset by 1 unit) and HD 100276 (*bottom*). The spectrum for HD 100276 has been rotationally broadened to make it comparable with HD 64760. The interstellar lines were also broadened in the process. Aside from the much stronger interstellar Lyα in HD 100276, the two spectra are remarkably similar.

$\lambda 1206$, N v $\lambda\lambda 1240$, C ii $\lambda\lambda 1335$, Si iv $\lambda\lambda 1400$, C iv $\lambda\lambda 1550$, and Al iii $\lambda\lambda 1860$ resonance lines, and the Si iii $\lambda\lambda 1300$ triplets. Wind activity was also detected in the C iii $\lambda\lambda 1175$ triplets and the S iii $\lambda 1190$ resonance line, but the signal-to-noise in these short-wavelength lines is so poor that they add little information to those shown. The individual profiles in the gray scales were normalized by a minimum absorption (maximum flux) spectrum, and a nearest neighbor time interpolation was used to place them onto a linear time grid (the individual spectra can be distinguished in the figures). Gaps appear whenever 3 or more hr elapsed between observations (see § 2). The minimum absorption template was obtained as follows: (1) The spectra were smoothed by a 50 km s^{-1} boxcar filter in the velocity direction. (2) Each velocity point of the smoothed spectra was replaced by the value determined from a 5 point quadratic fit in the time direction centered at that point. (3) This smoothed version of the spectra was searched at each velocity for the maximum flux at that velocity to produce the maximum flux (minimum absorption) template. The minimum absorption normalization causes all changes to appear as absorptions, so it is particularly convenient for a qualitative assessment of the observations. Since the normalizing spectra are nothing more than a display device, we ignore some of the rather unusual statistical characteristics of the minimum absorption spectra (see Kaper 1993). The Si iv lines show the activity most clearly, and are repeated in the last panel. The three vertical bars between the panels indicate the time spanned by three specific events described below. At the bottom of each panel we show the mean spectrum of the series, and two additional spectra that typify the minimum and maximum absorption that occurred during the series. SWP 47258, obtained during the quiescent period at the end of the run, represents the minimum

state, and the maximum state is represented by either SWP 47131 for the low ions (C ii and Al iii) and the Si iii triplets, or SWP 47155 for the high ions (Si iii, Si iv, N v, and C iv).

The first thing to notice in the Si iv gray scales is that the wind was continuously active throughout the run. The remnants of a high-velocity DAC can be seen at the beginning of the run, and two more appear during the first 36 hr. A complete description of the DACs is given in the next section.

There are three noteworthy, identifiable events that occurred during our monitoring campaign.

The main event.—This refers to the very strong increase in the absorption that began about 32 hr into the run. During the main event, the low-velocity absorption became stronger and *remained strong* for about an entire day. At the beginning of the main event, activity is present in the low ions, Al iii and C ii, the Si iii triplets, and even the C iii $\lambda 1247$ singlet (see Fig. 3 below). There is considerable activity in the C iv as well, but its close doublet spacing makes it difficult to interpret. The main event is first clearly seen at ~ -100 km s^{-1} in N v, Si iv, and C iv, and *at effectively zero velocity* (i.e., until the variability is lost in the interstellar absorption near $v = 0$) in the Si iii, C ii and Al iii resonance lines and the Si iii triplets (in § 5.1, we argue that the velocity at which the absorption is first detectable is probably related to the optical depth of the line near $v = 0$ km s^{-1}). Once the absorption strengthens, it progresses monotonically to higher velocity as time increases, except for the Al iii doublet, where the onset of the event seems to be preceded by an inflow! In addition to the lines shown in the gray scales, the strong C iii $\lambda 1247$ singlet also exhibited variability associated with the main event. Figure 3 compares the mean profiles of three spectra near the beginning of the main event (SWP 47140, 47143, and 47146—*solid curve*) and several obtained
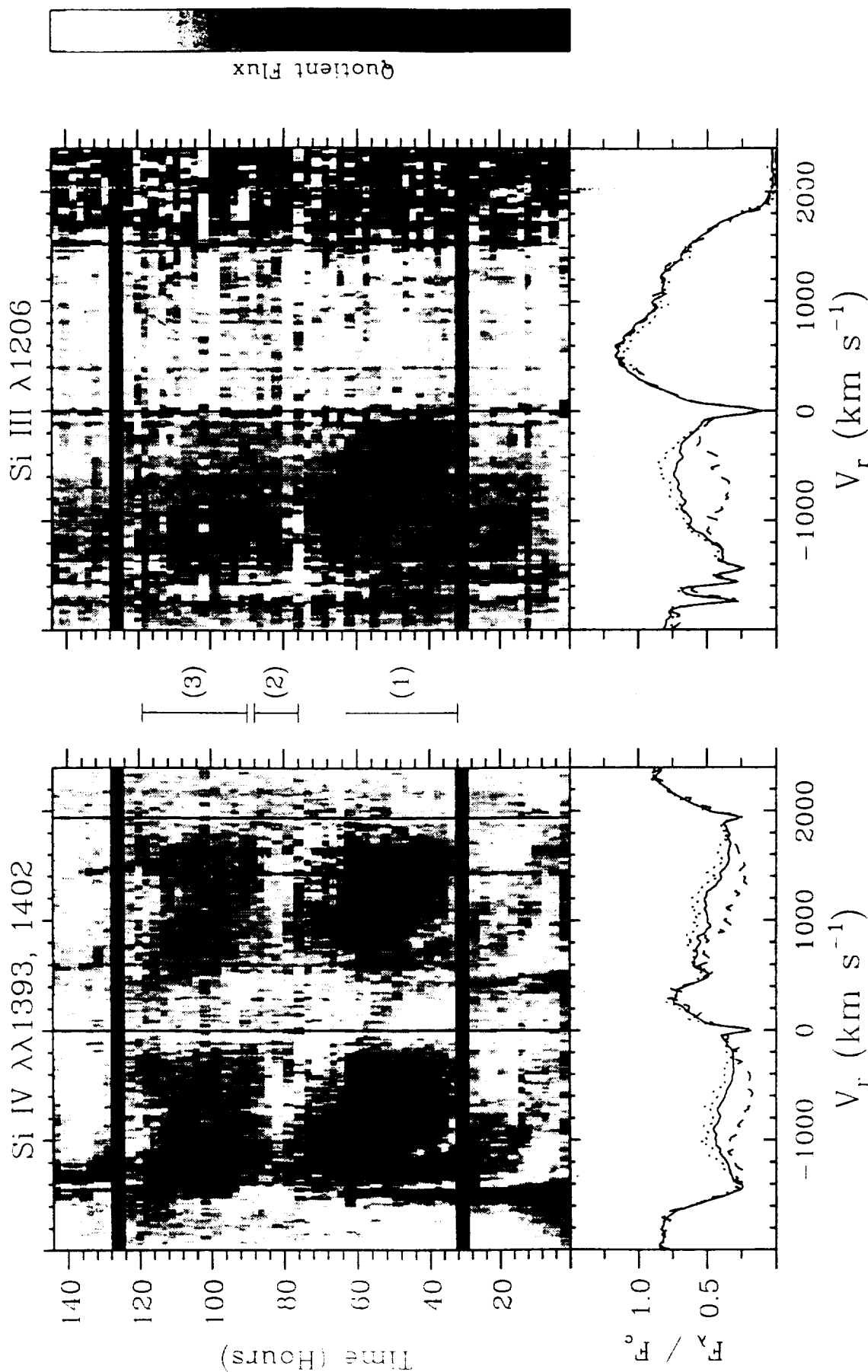
FIG. 2.—Gray-scale plots of the wind lines and the Si III λλ1300 triplets in HD 64760. The identification for each plot is given above it. Time increases upward, and is labeled by the number of hours since the beginning of the series. The individual spectra were normalized by a minimum absorption (maximum flux) spectrum so that all changes appear as absorptions. Nearest neighbor interpolation was used to place the spectra on a linear time grid, and gaps appear whenever more than 3 hr elapsed between exposures. The rest wavelengths of the lines are shown as vertical lines. The gray-scale bar at the side of each pair shows the scaling used, where the maximum is always 1.0 and minimum limits depend upon the line. These are 0.5 for Si III and N V, 0.6 for Si IV, 0.3 for C IV, and 0.8 for all the others. The vertical bars between the panels indicate the time spanned by three specific events described in § 4.1: (1) the main event, (2) the weakening period, and (3) the second major event.

The bottom of each panel shows the mean spectrum for that ion and spectra representing the maximum and minimum total absorption during the run. The minimum spectrum used for all the lines is SWP 47258. The maximum absorption spectrum shown depends upon the line. SWP 47155, which occurs during the maximum strength of the main event, is used for Si III λ1206, N V, Si IV, and C IV, and SWP 47131, which occurs at the beginning of the main event, is used for the other lines.
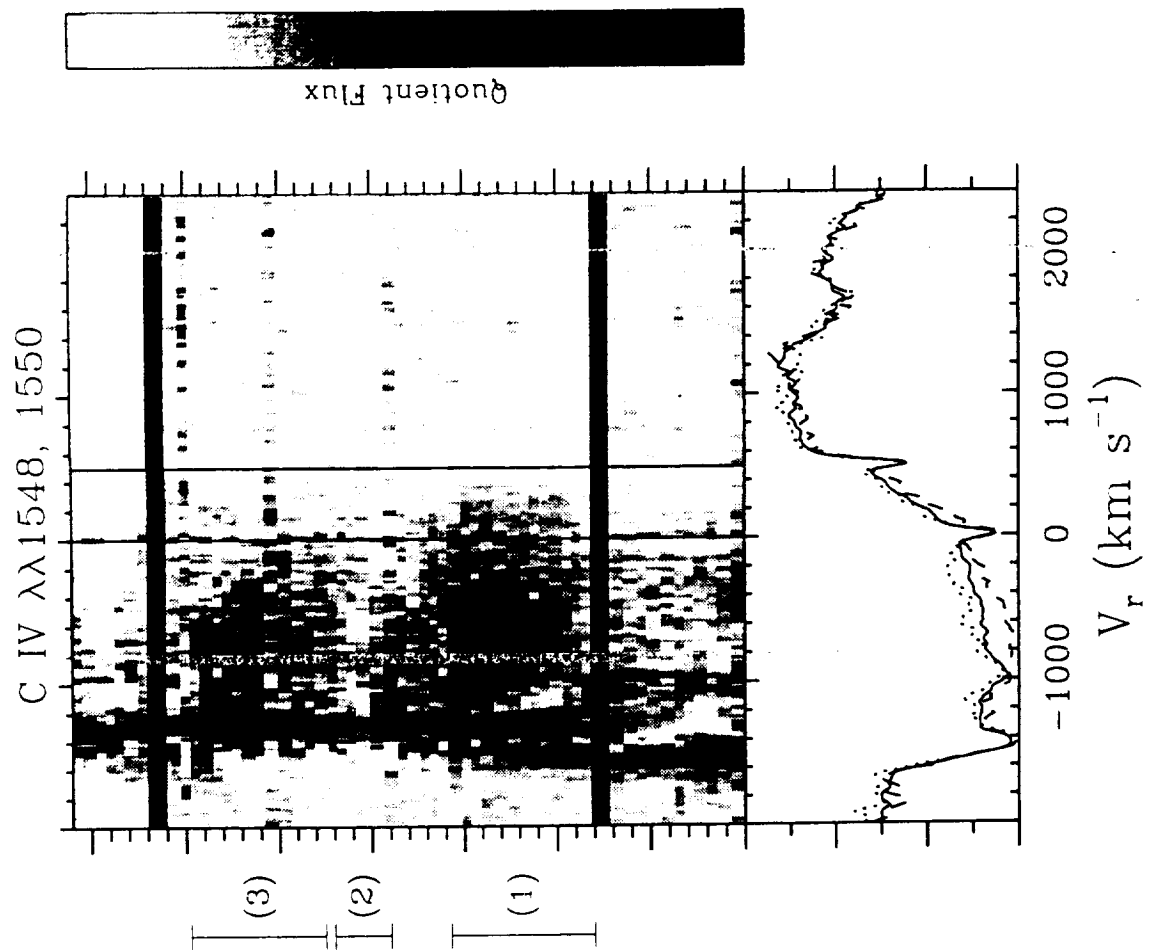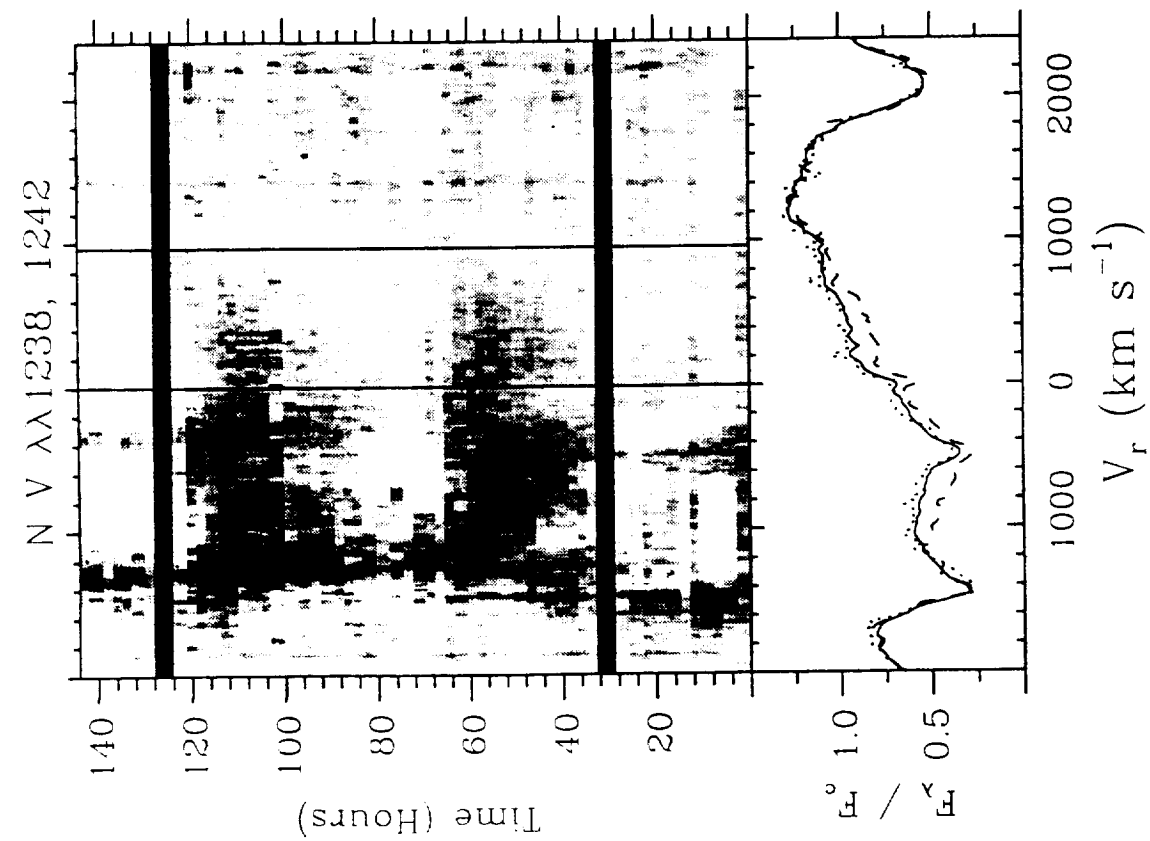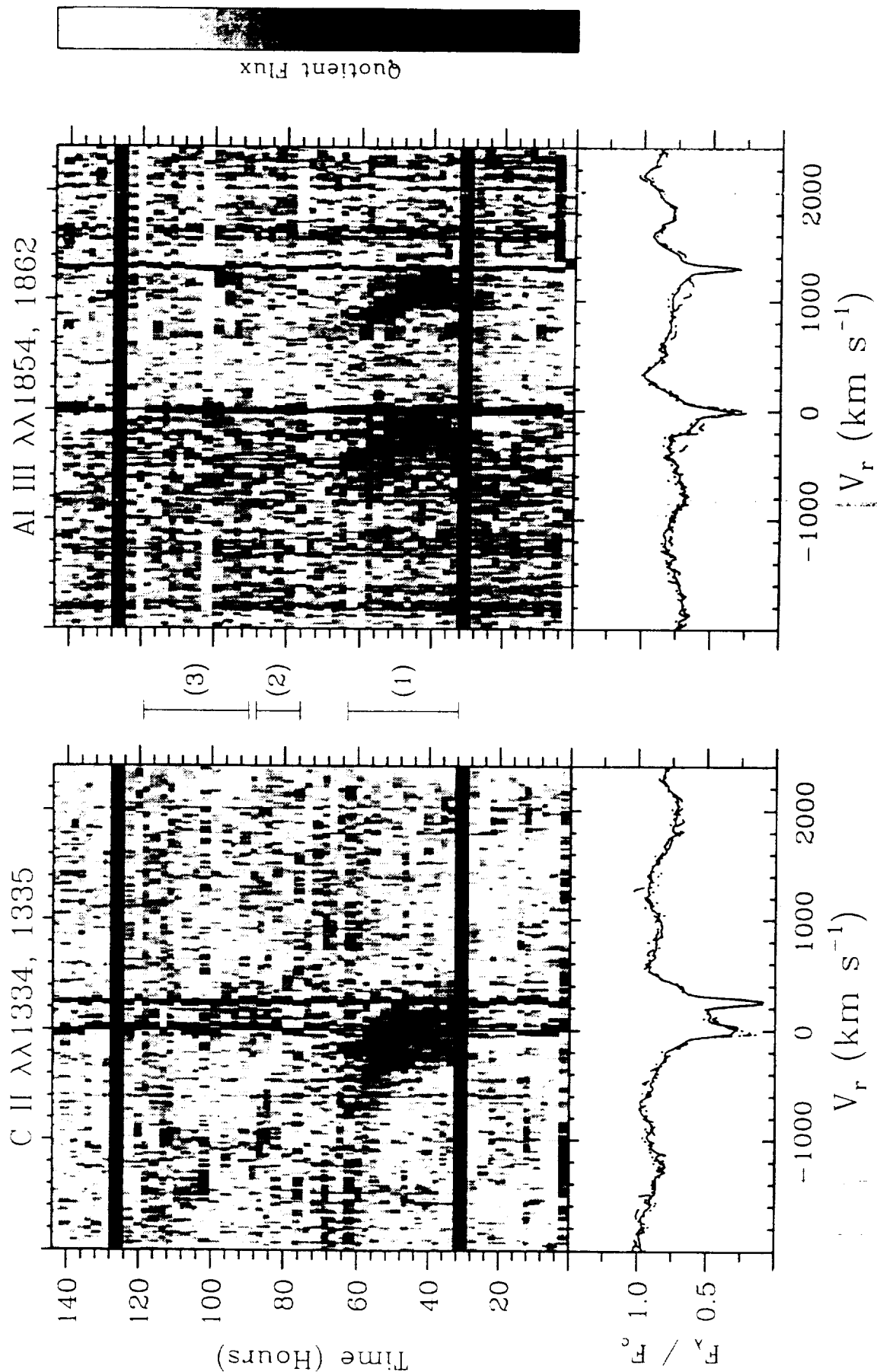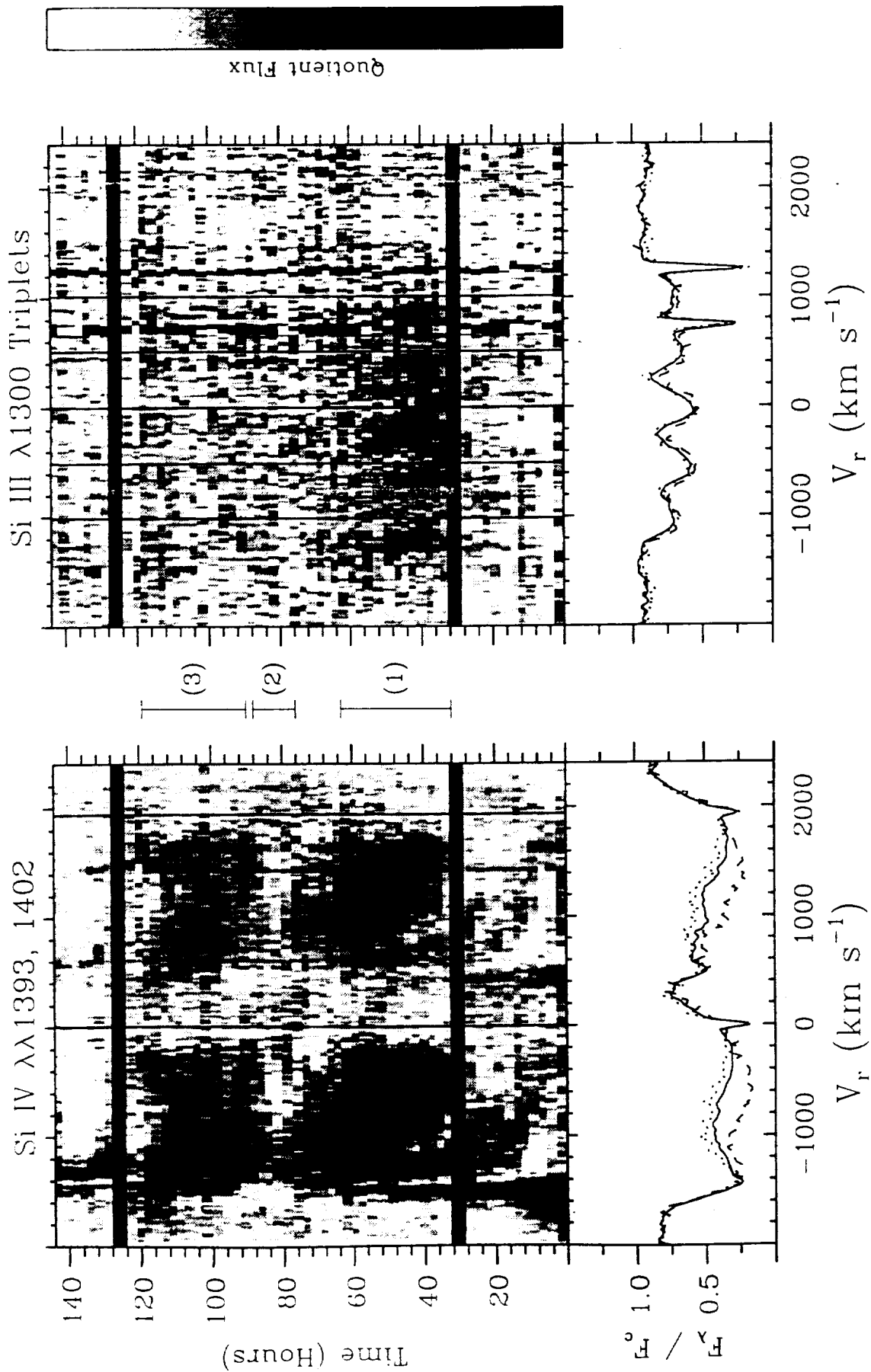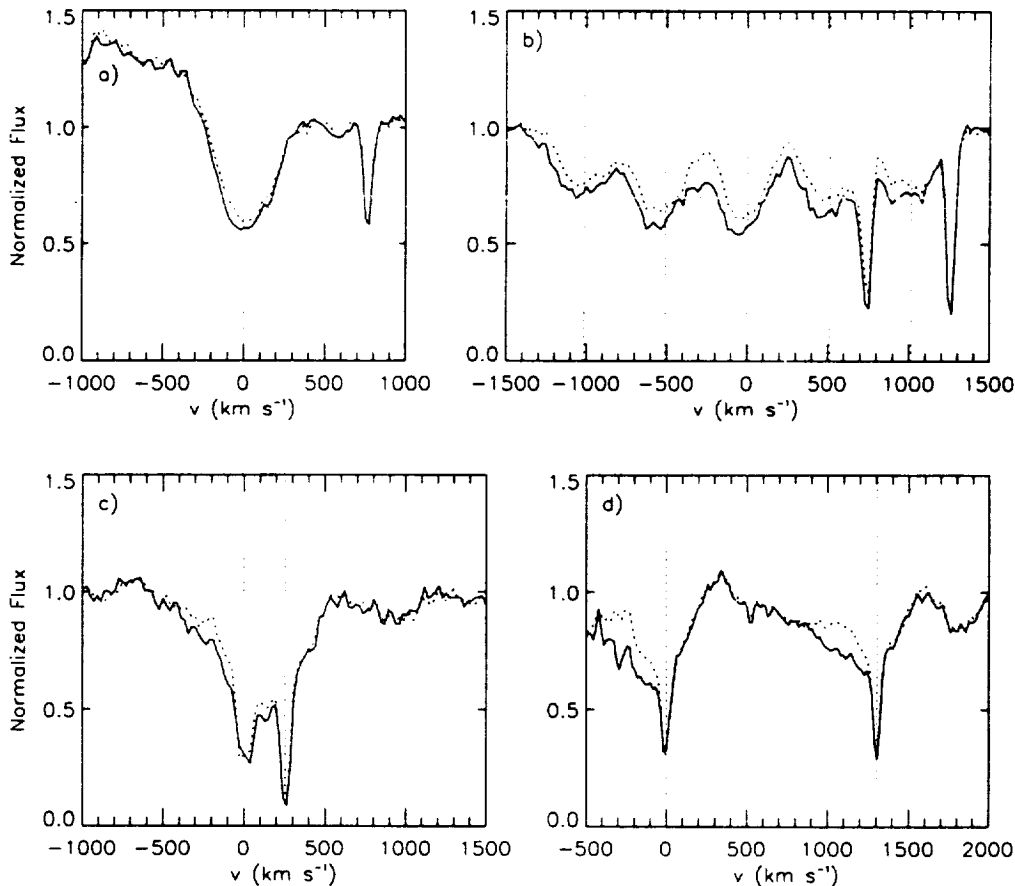
846

Fig. 2—Continued

847

Fig. 2—Continued

848

Fig. 2—*Continued*

FIG. 3.—Comparison of mean profiles for (a) the C III λ1247 singlet, (b) the Si III λ 1300 triplets, (c) the C II λλ1335 resonance doublet, and (d) the Al III λλ1860 resonance doublet. The solid curves are the means of three spectra near the beginning of the "main event" (SWP 47140, 47143, and 47146) and the dashed curves are the mean of six spectra obtained during the quiescent period near the end of the run (SWP 47246–47261).

near the end of the run when the wind was at its most quiescent (SWP 47146–47161—*dashed curve*). C III λ1247 shifted by ∼ 10 km s^{-1} and noticeably strengthened at the beginning of the main event, as did the Si III λλ1300 triplets. Figure 3 also clearly shows how variability in the violet absorption of the low ion lines is present to the lowest velocities observable before the lines become dominated by interstellar absorption.

The weakening period.—This refers to the sudden, general weakening in the absorption that occurs about 72 hr into the series. (This feature shows up particularly well in Figure 4, below, which presents Si IV λ1393 in a larger format). At this time, the absorption associated with the main event suddenly weakens in all of the high ions. It is especially pronounced in the Si III and IV series. This is extremely puzzling since one would expect the absorption to become narrower and deeper as it evolved toward higher velocity.

The second major event.—A little before 90 hr into the series there seems to be an overall strengthening in the absorption across a broad band of velocities simultaneously. However, this may be the result of a confluence of several weak, disorganized DACs (see § 4.2).

Finally, we point out that there is no compelling evidence for variability in the red emission wings of the P Cygni profiles. However, this should not be too surprising at the signal-to-noise afforded by *IUE* (see § 5.1).

In summary, the time series contains evidence suggestive of: gas emanating from *very near* $v = 0$ km s^{-1} (in the low ions

during the main event); a distinct correlation between variability in the Si III λλ1300 triplets, the strong C III λ1247 singlet, and the onset of extremely strong wind activity, indicating a connection between photospheric and wind activity; large-scale spatial structure in the wind (the simultaneous weakening of the wind lines over a wide range of velocities during the weakening period); and perhaps even surface features (the long time coherence of the low-velocity outflow during the main event). Throughout the following sections, we will repeatedly return to these ideas in an attempt to bolster them.

4.2. DAC Analysis

It is useful to derive some quantitative measures of the DACs that can be identified in Figure 2. Following the analyses of DACs in other hot stars (see, e.g., references in § 1), we first modeled the time-dependent behavior of the Si IV λλ1393.76, 1402.77 and Si III λ1206.51 wind lines in terms of sequential episodes of discrete optical depth enhancements. Model Gaussian profiles with multiple components were fitted, by least squares, to the residual absorption spectra obtained by dividing the observed P Cygni profiles by the adopted minimum absorption (maximum flux) templates (§ 4.1). The central velocities, line widths, and line-center optical depths are the fitting parameters used to match the observed DAC spectra. (Although some of these discrete features can also be traced in C IV and N V—see, e.g., Fig. 2—the smaller doublet separation of these lines leads to severe blending between
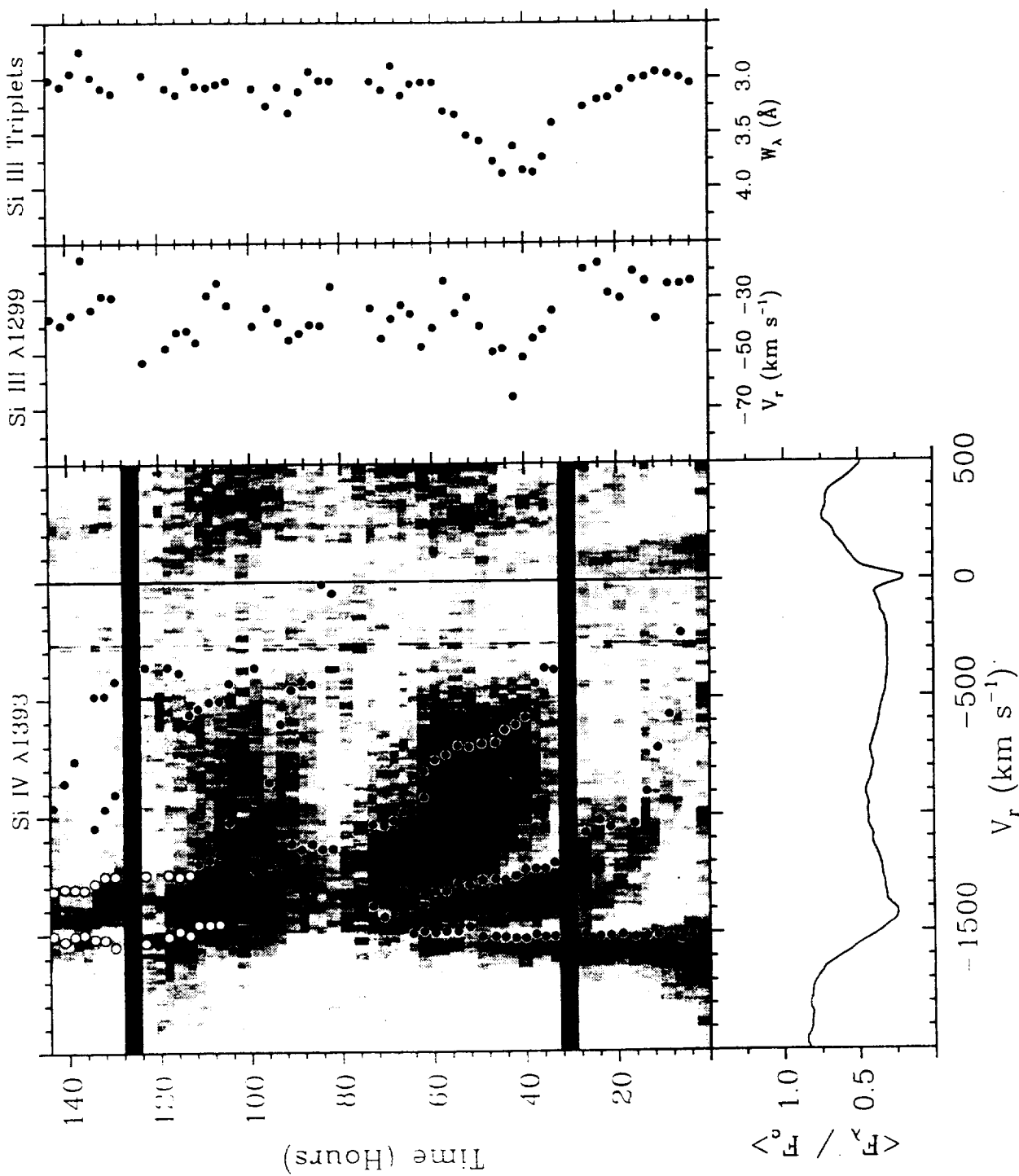
FIG. 4.—The left panel is a gray-scale plot (as in Fig. 2) of the Si IV λ1393 line with the mean profile shown beneath it. The positions and motions of the different DACs discussed in the text are superposed upon the gray scale. In two instances, DACs seem to merge, and it is not obvious which of the initial DACs is responsible for the later absorption. In these cases, we distinguish the extensions of the initial DACs as open circles. The central panel shows the central position of the λ1299 component of the Si III λ1300 triplet and the right panel shows the total strength of the entire Si III λ1300 multiplet.

broad DACs from different doublet components, and greatly increases the uncertainties in profile fitting.)

As noted earlier, the stellar wind of HD 64760 was continually active during the ~ 6 days of our *IUE* monitoring in 1993 March. This activity may be interpreted in terms of at least six sequential episodes, each characterized by a localized increase in optical depth and subsequent migration to blueward velocities. The individual properties of these six DACs are outlined below. The adopted central velocities of these features are plotted as a function of time in Figure 4, where they are superposed on a gray-scale representation of the time-variable line profile behavior. In two instances, DACs seem to merge, and it is not obvious which of the initial DACs is responsible for the later absorption. In these cases, we distinguish the extensions of the initial DACs as open circles. Occasionally there is an apparent "mismatch" between the gray-scale "tracks," which the eye follows, and the "dots" representing the central positions of the Gaussians. This is an artifact of modeling inherently asymmetric profiles with symmetric Gaussians. Overall, "realistic" errors in the DAC central velocities and central optical depths are ~ 20–30 km s^{-1}, and 10%–20%, respectively.

Figure 4 also shows the behavior of the Si III $\lambda\lambda 1300$ triplets throughout the series. The first panel to the right of the gray scale gives the time dependence of the central position of the $\lambda 1299$ component of the multiplet and the panel on the far right shows the time dependence of the equivalent width of the entire multiplet.

DAC (1).—A high-velocity "narrow absorption component" (FWHM ~ 200 km s^{-1}) is conspicuous at the shortward edge of the Si IV profiles throughout the 6 days of observations. Although its strength decreases after $\Delta t \sim 70$ hr (see, e.g., Figs. 2 and 4), it can still be identified in the Si IV line profiles during the ~ 20 hr following the start of the "weakening period." (Although this DAC is also evident in Si III, its appearance is somewhat masked by the presence of strong N I interstellar absorption lines at 1200 Å). Further evidence for the longevity of this feature may come from the fact that narrow absorption features are seen at similar velocities in the archival spectra of HD 64760, which span almost 14 yr.

DAC (2).—The second DAC to appear in our time series provides a particularly fine example of a feature migrating blueward across almost the entire extended absorption trough. It is first detected at ~ -250 km s^{-1} (SWP 47100, $\Delta t \sim 8$ hr), and progresses to blueward of -1400 km s^{-1} over ~ 65 hr, where it weakens considerably (§ 4.1). The acceleration of the feature varies from $\sim 2.2 \times 10^{-2}$ km s^{-2} at $\sim 0.3 v_{\infty}$ to less than 2.0×10^{-3} km s^{-2} at more than $0.85 v_{\infty}$. Similar to migrating DACs in other early-type stars, the FWHM of this feature exhibits a systematic dependence on central velocity; i.e., increases initially to about 650 km s^{-1}, and then gradually narrows to ~ 125 km s^{-1} near the blue edge of the profile.

DAC (3).—This is the "main event" identified in § 4.1. It represents the strongest and broadest (in velocity) optical depth change observed in all the wind-formed lines of HD 64760, including Si IV, Si III $\lambda 1206$, N V, and C IV. The occurrence of this event also coincides with the largest activity seen in Si III $\lambda 1300$, C III $\lambda 1247$ and Al III $\lambda\lambda 1855$, 1863 (see § 4.1). In fact, *the only time that distinct variability is observed in the low ions, the triplets and the C III singlet appears to be related to the main event* (see Fig. 2). In particular, the central position of the Si III $\lambda 1299$ component of the triplet shifted by more than -15 km s^{-1} and the equivalent width of the entire

multiplet increased by more than 25% (Fig. 4). The exceptional nature of this "event" casts some doubt as to whether it should be regarded as a "DAC," and whether it should be grouped with the other features outlined in this section. Furthermore, the Gaussian model profiles do not match the observed shapes of this feature very well, since the (residual) DAC profiles have considerable asymmetries (mostly on the redward side). Our measured velocities are therefore less reliable in this case. The Si IV central velocity of this feature changes from ~ -380 km s^{-1} at initial identification (SWP 47128) to -1230 km s^{-1} about 70 hr later. We estimate a mean acceleration of $\sim 7 \times 10^{-3}$ km s^{-2}. Although the corresponding Si III central velocities adopted are typically 100–200 km s^{-1} less than in Si IV, this apparent difference likely reflects uncertainties arising from the asymmetries in the DAC profiles. The "main event" has a maximum width in Si IV of ~ 1200 km s^{-1} (i.e., more than 75% of the total P Cygni profile absorption width!); this is quite exceptional, and is not a typical DAC property. The total Si IV ion column density due to this feature may be as high as 4×10^{14} cm^{-2} (assuming locally plane-parallel geometry).

DAC (4).—The next sequential DAC in our time series data is initially detected at very low velocities, down to less than $0.05 v_{\infty}$, in Si IV and Si III. Its initial migration to -1200 km s^{-1} occurs during the period when the high-velocity DACs (1 and 2) are weakening considerably (see, e.g., Figs. 2 and 4). The identification of this discrete feature is very ambiguous after $\Delta t \sim 110$ hr, due to increased blending with the previous migrating DAC. The mean DAC FWHM in Si IV is ~ 700 km s^{-1}, with its acceleration changing between $\sim 1.5 \times 10^{-2}$ km s^{-2} at less than $0.2 v_{\infty}$, to less than 3×10^{-3} km s^{-2} at greater than $0.8 v_{\infty}$.

DAC (5).—This is a weak episode in Si IV, which is not traced in Si III. The absorption enhancement is first apparent at $\Delta t \sim 100$ hr with a central velocity ~ -350 km s^{-1}. The DAC migrates blueward to -1050 km s^{-1} over ~ 36 hr. It has a mean acceleration of $\sim 6 \times 10^{-3}$ km s^{-2} at $\sim 0.5 v_{\infty}$.

DAC (6).—Another rather weak, shallow—but systematic—enhancement is noted toward the end of our time series observations. It moves from -300 km s^{-1} ($\Delta t \sim 116$ hr) to -1000 km s^{-1} over ~ 30 hr. Our analysis has recorded therefore the initial appearance of five DACs (including the "main event") in HD 64760 over ~ 4.5 days, with an approximate recurrence rate of ~ 22 hr. This recurrence timescale for the DACs and their observed accelerations in HD 64760 are broadly consistent with previous indications that the timescale for wind activity in early-type stars is related to the stellar rotation period. This "relation" is still poorly defined, though UV observations support a trend of faster developing, more frequent DACs, with increasing $v \sin i$ (see, e.g., Prinja 1988; Henrichs et al. 1988; Kaper 1993). A detailed examination of the wind lines in HD 64760 as a function of rotation rate is frustrated by the fact that our UV data set only extends over less than two estimated rotation periods. We note, meanwhile, that the precise patterns of velocity, width, and strength of the individual DACs as a function of time do *not* repeat between successive episodes in our data. Each DAC is apparently rather different, and we find no evidence to indicate that a given (stable) wind structure or perturbation has entered the line of sight more than once during ~ 6 days of monitoring. The observed acceleration of the DACs in HD 64760, and its time dependence, are also variable between different features. Accelerations at a central velocity of $\sim 0.5 v_{x}$, for example, range

from $\sim 6 \times 10^{-3}$ km s^{-2} [DACs (3) and (5)] to $\sim 1.4 \times 10^{-2}$ km s^{-2} [DAC (2)]. In comparison, steady state wind models, with "$\beta = 1$" type velocity laws, predict an acceleration of $\sim 2 \times 10^{-2}$ km s^{-2} at $0.5v_x$ for HD 64760. The apparent slow acceleration of the DACs is now an established requisite for hydrodynamical simulations of wind perturbations that yield substantial spatial structure.

Under the assumption of locally plane-parallel geometry, the Gaussian fits to the residual DAC profiles in the resonance lines (see, e.g., Prinja & Howarth 1986) indicate that the observed Si IV/Si III relative ion fractions in individual features vary by up to a factor of 4 as a function of velocity. DACs (2), (3), and (4) represent the clearest examples of variable localized optical depth enhancements in our data set, and in each case the ratio of N(Si IV)/N(Si III) increases initially to a maximum occurring at $\sim 700 \pm 100$ km s^{-1}, and then drops as the features migrate to higher velocities. The mean ratios for DACs (2), (3), and (4) are $\sim 4.3 \pm 1.1$, 4.2 ± 2.6, and 2.7 ± 0.4, respectively.

Finally, in several cases unaccounted absorption is present in addition to the DACs and the "underlying" maximum flux template. This is especially true during the "main event" and toward the end of the observing run ($\Delta t > 120$ hr). Although the six DACs clearly represent the most substantial structures observed in these wind profiles, there may also be small-scale, perhaps more irregular, wind fluctuations that have not been documented here.

5. WIND LINE MODELING

Our ultimate goals are to determine how the wind activity arises and evolves. To accomplish this, we must determine how much material is in the wind at any given time and how its ionization changes with activity. To perform such an analysis requires us to derive column densities or, equivalently, optical depths from the observations.

5.1. Preliminaries

We begin with a qualitative overview of the problem in order to clarify several points to be made in the detailed analysis. For this purpose, we adopt a simple model for the observations (which is appropriate for a singlet or that portion of the violet component of a doublet that is free of overlap) that expresses the observed flux at a given wavelength, λ, as the sum of components. The first is the intrinsic stellar flux, $f_0(\lambda)$, extinguished by variable absorption due to the wind, $e^{-\tau_w(\lambda, t)}$, and the second is the time-independent scattered light from the wind that contributes to the flux at λ, $f_e(\lambda)$. Although τ_w is an ill-defined average of τ_{rad} (or τ_1 in Lamers, Cerruti-Sola, & Perinotto 1987 notation) integrated across the face of the star and f_e is certainly time dependent at some level (but fairly stable at the signal-to-noise of IUE), this simple model still reveals the major problems confronting us.

The observed profile is given by

$$f(\lambda, t) = f_0(\lambda)e^{-\tau_w(\lambda, t)} + f_e(\lambda) . \tag{1}$$

The constant projected velocity surfaces for a monotonically expanding wind (see, e.g., Fig. 2 of Lucy 1971) require that *all* of the diffuse emission that contributes to the flux at a given projected velocity, v_z, emanates from radii that are *larger* than the radius where the absorption occurs. Therefore, the scattered light contribution at λ cannot interact with the same gas that is responsible for the absorption at λ. Notice that while an increased ionic abundance at a particular velocity, v, and pre-

sumably a particular radius, r, absorbs strongly at v, emission from this shell at r is redistributed over all projected velocities between $\pm v$. This emission will be weakened further if it is occulted by the star or if its spatial extent is limited. In addition, any impact that an inhomogeneity may have on the emission at some projected velocity $v_z < v$ is seen against emission originating from a broad region of the wind (i.e., the entire constant velocity surface), spanning all velocities from v_z to v_∞. Owing to these physical and geometrical effects, it will generally be much more difficult to detect emission variability associated with variable absorption features.

We would like to estimate the physical quantity, $\tau_w(\lambda, t)$, since it contains the column density information we seek. Unfortunately, τ_w is intertwined with the diffuse emission term, $f_e(\lambda)$, which can be very large compared to $f_0(\lambda)e^{-\tau_w(\lambda, t)}$, especially at low velocity. The fits to the wind lines shown in Figure 5 (below) demonstrate the effect. They are broken into two portions, corresponding to the terms in equation (1). Referring to the fits, we see that in most cases nearly all of the flux at low velocity is due to light scattered toward the observer from larger radii. Consequently, *it is not surprising that DACs are rarely observed at low velocity*. In thick wind lines, there is very little transmitted flux available at low velocity for an inhomogeneity in the wind to absorb. So even if the inhomogeneity has an infinite optical depth, it can only absorb a small portion of the total flux, the remainder being due to scattered light. Consequently, the velocity at which a feature first appears has as much to do with the optical depth of the line as it does with the presence of an inhomogeneity in the wind flow.

Returning to our goal of determining optical depths, even the assumption that most of the terms are time independent does not help. Subtracting the time average at each wavelength eliminates the $f_e(\lambda)$ term, but still does not isolate τ_w. Taking the time derivative also eliminates the $f_e(\lambda)$, assumed to be time independent, viz.,

$$\frac{df}{dt} = -f_0(\lambda)e^{-\tau_w(\lambda, t)}\frac{d\tau_w}{dt} . \tag{2}$$

Unfortunately, neither the optical depth or its derivative can be easily isolated. The derivative does possess one useful property. It changes sign whenever $d\tau_w/dt$ changes sign, so it can be used to examine the onset of changes in the optical depths.

Mathematically, the problem is simple. We would like to take a logarithm in order to obtain τ_w, but there is also an additive term that cannot be removed empirically. Thus, there does not seem to be an obvious way to extract the column density information without somehow "correcting" the observations for f_e, and this requires at least some reliance upon a model.

5.2. Profile Fitting

To obtain quantitative results, and to help us understand the different contributions to the wind profiles, we modeled the Si III, N V, Si IV, and C IV wind lines using the Sobolev with exact integration method (SEI) described by Lamers et al. (1987). The Si III and N V lines in HD 64760 were corrected for 1.4×10^{20} cm^2 Lyα absorption using a simple Lorentzian reconstruction (see Bohlin 1975).

The models require the following three input functions.

Velocity law.—We assume a standard β law for the wind of the form (Lamers et al. 1987)

$$w = w_0 + (1 - w_0)(1 + 1/x)^\beta . \tag{3}$$
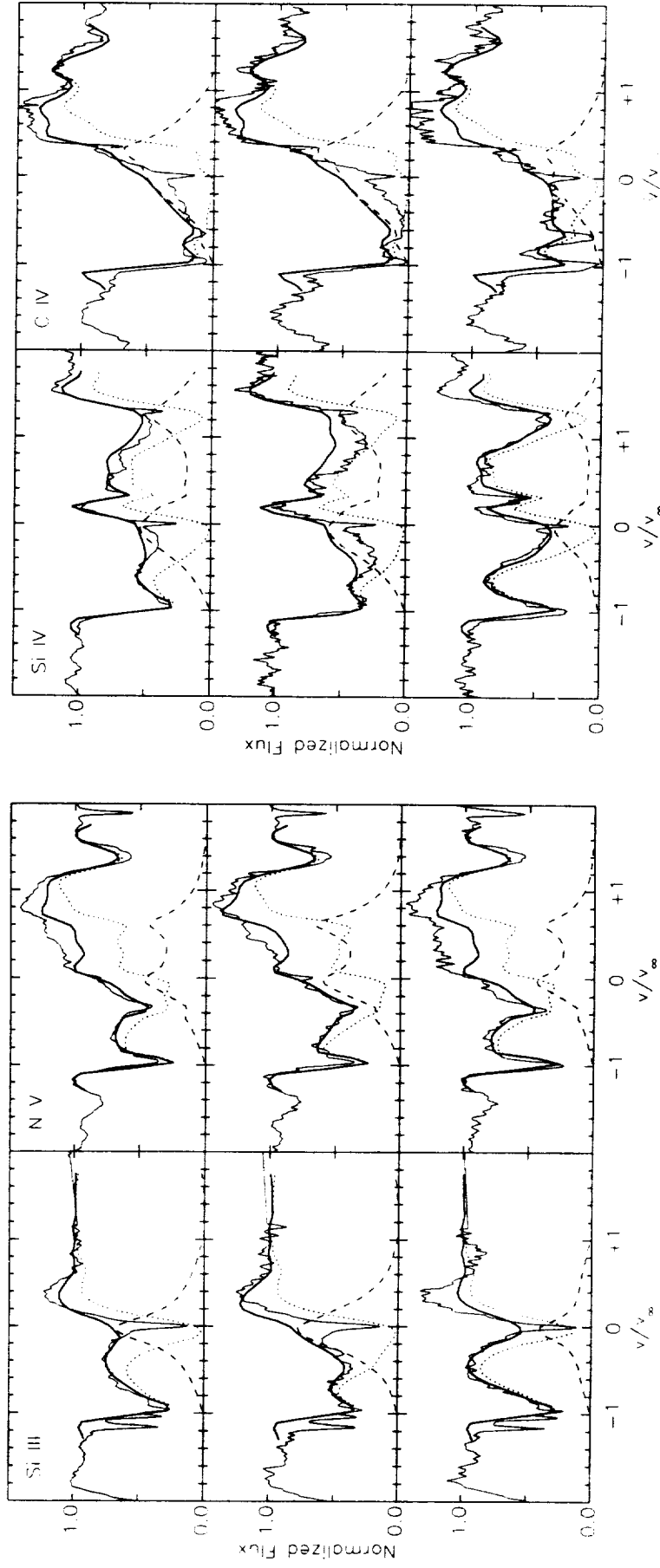
FIG. 5.—Model fits to the minimum (bottom), maximum (middle) and mean (top) profiles vs. normalized velocity (where $v_\infty = 1500$ km s^{-1}) of Si III $\lambda1206$, N V $\lambda\lambda1240$, Si IV $\lambda\lambda1400$ and C IV $\lambda\lambda1550$. In each case, the observed (thin line) and model profile (thick line) are shown, as are the contributions to the profiles from the transmitted (dotted line) and scattered light (dashed line).

where $w = v/v_\infty$ and $x = r/R$, where R is the stellar radius. We select $\beta = 1.0$ and $w_0 = 0.01$. The profiles are insensitive to changes in β for $0.5 \leq \beta \leq 2.0$. The relatively sharp blue edges of the wind profiles provide a well-defined estimate for $v_\infty \simeq 1500$ km s^{-1} and constrain the value of the small-scale velocity dispersion parameter, w_D, to lie between 0.05–0.10, and a value of 0.07 was adopted (implying a localized velocity dispersion of ~ 100 km s^{-1}). Our model-dependent value of v_∞ can be compared to empirical determinations. Groenewegen, Lamers, & Pauldrach (1989) suggest that $v_\infty = (0.87 \pm 0.05)v_{\rm edge}$, where the edge velocity is determined from the point at which a saturated profile rejoins the continuum. For HD 64760, the C IV profile is the only one approaching saturation, and it has a $v_{\rm edge} = -1650$ km s^{-1}, which implies that $v_\infty = -1436 \pm 99$ km s^{-1}, consistent with our estimate. Howarth & Prinja (1989) suggest that the largest observed DAC velocity is the best estimate for v_∞. As can be seen from Figure 4, the highest velocities attained by DACs were between -1500 and -1550 km s^{-1}, again in good agreement with the adopted terminal velocity.

Input photospheric spectrum.—For the Si IV, C IV, and N V lines, we used the profiles of the B0.2 III star HD 164340. The overall match between the photospheric features in this star and HD 64760 is very good, and its resonance lines are only slightly affected by wind absorption. Because HD 164340 has a small $v \sin i$ we rotationally broadened its spectrum by an additional 230 km s^{-1} using a simple convolution without limb darkening (we did not "correct" for the weak interstellar contributions, as these only affect the line cores where the flux is already small). Because of its relatively large Lyα column density $(1.4 \times 10^{20}$ cm$^2)$ the "reconstructed" Si III $\lambda 1206$ line in HD 164340 is highly uncertain. Therefore, we employed a spectrum of the B0.5 III $(v \sin i = 35$ km s$^{-1})$ star β Cru (corrected for 9.0×10^{19} cm^2 of Lyα absorption) for this line. In this case, we first interpolated across the strong N I $\lambda 1199.55$, 1200.22, and 1200.71 interstellar features in the vicinity of Si III $\lambda 1206$. Although there is probably a relatively strong interstellar contribution to the Si III $\lambda 1206$, it is not possible to disentangle it from the photospheric component. The spectrum was then rotationally broadened by an additional 230 km s^{-1}. Although the photospheric features do not match those in HD 64760 as well as HD 164340, it should be adequate for our purposes.

Wind optical depth.—The radial optical depth of the wind as a function of w is given by $\tau_{\rm rad}(w)$. While $w_0 \leq w(x) \leq 1$, it maps onto projected velocities over the interval $-1 \leq w_z \leq 1$ of the observed profile. We modeled $\tau_{\rm rad}(w)$ as a number of independent bins whose magnitudes and positions were adjusted to obtain the fit. This approach was preferred to the usual opacity laws, since the motivation for the latter depends upon the wind being in steady state, which is clearly not the case. With the parameters in the velocity law and photospheric inputs fixed, $\tau_{\rm rad}(w)$ is the only free parameter. This leads to a very simple line-fitting scheme. It relies on the following property of the Sobolev approximation for a wind with a monotonically increasing velocity law (ignoring turbulence): as mentioned in § 5.1, the contributions to the wind profile at a given normalized velocity, $-w_z$, are due to the emission and absorption of ions distributed over a constant velocity surface. Therefore, ions which contribute to the flux at $-w_z$ are all located at distances $\geq r(w)$, with the equality holding only at the single point nearest the star. As a result, we can begin by assuming that $\tau_{\rm rad}(1 \geq w \geq 1 - \Delta w_1) \equiv$ constant $= \tau_1$ and fit the profile

between $-1 \leq w_z \leq -1 + \Delta w_1$ to determine τ_1. The quality of the fit obtained in the interval $-1 \leq w_z \leq -1 + \Delta w_1$ is fixed, and cannot be affected by the values selected for $\tau_{\rm rad}(w < 1 - \Delta w_1)$. Next, we adjust the value of $\tau_2 \equiv \tau_{\rm rad}(1 - \Delta w_1 \geq w \geq 1 - \Delta w_1 - \Delta w_2)$ to fit the profile between $-1 + \Delta w_1 \leq w_z \leq -1 + \Delta w_1 + \Delta w_2$. Again, the quality of the fit cannot be affected by the values selected for $\tau_{\rm rad}$ at smaller values of w, i.e., $\tau_{\rm rad}(w < 1 - \Delta w_1 - \Delta w_2)$. This procedure is then repeated, and the profile is fitted, bin by bin, progressing to less and less negative velocities, each time determining the value of τ_n between

$$1 - \sum_{i=1}^{n-1} \Delta w_i$$

and

$$1 - \sum_{i=1}^{n} \Delta w_i \, .$$

Once the fit is determined at high velocity, the contribution to the scattered light at lower velocities cannot be changed. If the low-velocity portion of the profile determined from fitting the high-velocity region is inconsistent with the observations (i.e., if fitting the high-velocity portion of the profile produces so much scattered light at low velocity that no value of $\tau_{\rm rad}$ can reproduce the observed profile), then nothing can be done. Such a failure implies a fundamental fault in either the input photospheric spectrum, the choice of velocity law, or the basic assumptions of the model (e.g., spherical symmetry, or the Sobolev approximation itself). If all goes well, the fitting procedure produces a histogram representation of $\tau_{\rm rad}(w)$. We modeled the minimum (smallest integrated equivalent width) and maximum (largest integrated equivalent width) absorption states of all the available spectra and the mean spectrum of the time series for each line. Examining these three cases will help us assess systematic behavior in the fits. For the minimum spectrum, we used a spectrum not in the series, SWP 7718 (obtained 1980 January 20) and for the maximum we used SWP 47155. We realize that the fit to the series mean spectrum is not representative of the wind at any given instant because the relationship between $\tau_{\rm rad}$ and the fluxes is not linear. However, it has the advantage of a large signal-to-noise, and it represents the best estimate for the mean wind conditions available.

5.3. Model Fits

Figure 5 shows the fits to minimum, mean and maximum profiles of the strong wind lines along with the contributions to the profiles by the transmitted and scattered light (see eq. [1]). Figures 6 and 7 show the photospheric contributions and the $\tau_{\rm rad}(w)$ used for each fit. Table 3 lists the values of $\dot{M} q_i$, the mass-loss times the ion fraction, derived from the fits to the mean, minimum and maximum spectra for each line at $0.5r_x$

TABLE 3

Ion Fractions at $v = 0.5r_x$

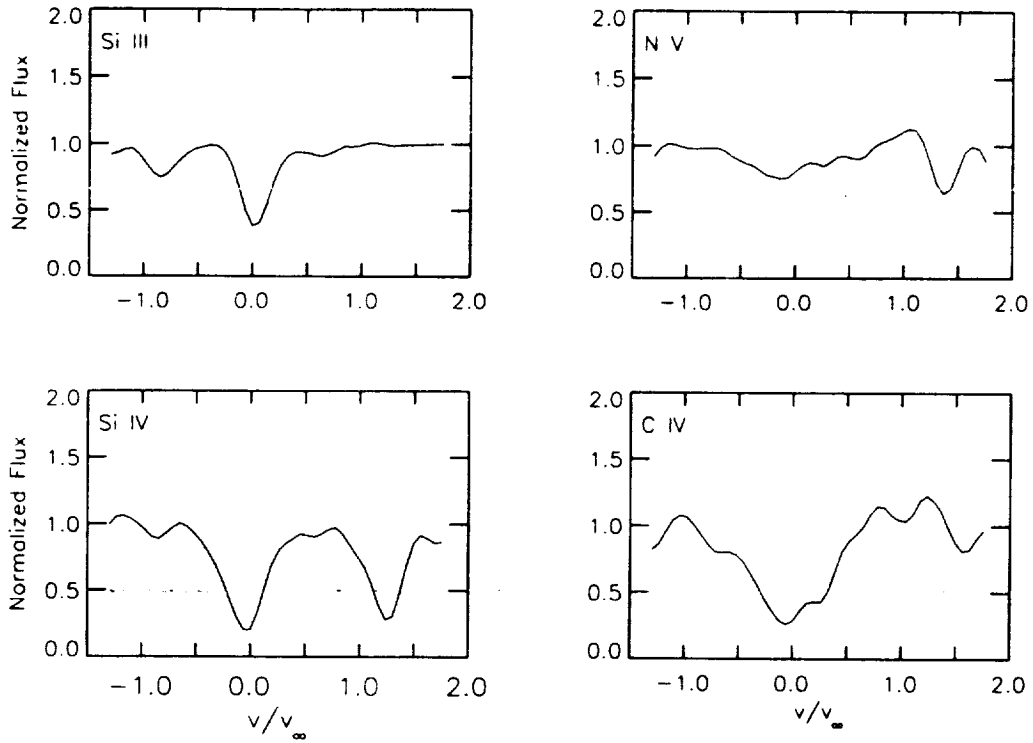| Ion	$\dot{M}_{-6}q_i$ Mean	$\dot{M}_{-6}q_i$ Min	$\dot{M}_{-6}q_i$ Max
Si III	2.0×10^{-4}	4.1×10^{-5}	5.7×10^{-4}
Si IV	1.3×10^{-3}	3.3×10^{-4}	2.2×10^{-3}
C IV	4.8×10^{-4}	2.3×10^{-4}	5.3×10^{-4}
N V	8.2×10^{-4}	6.9×10^{-4}	1.5×10^{-5}

FIG. 6.—Photospheric input profiles for the fits shown in Fig. 5, for Si III λ1206 (*top left*), N V λλ1240 (*top right*), Si IV λλ1400 (*bottom left*), and C IV λλ1550 (*bottom right*). The N V, Si IV, and C IV profiles are from the B0.2 III star HD 164340, and have been rotationally broadened to match HD 64760. For Si III, we used the B0.5 III star β Cru. In this case, the interstellar N I lines and Lyα were corrected in the line before the line was broadened.
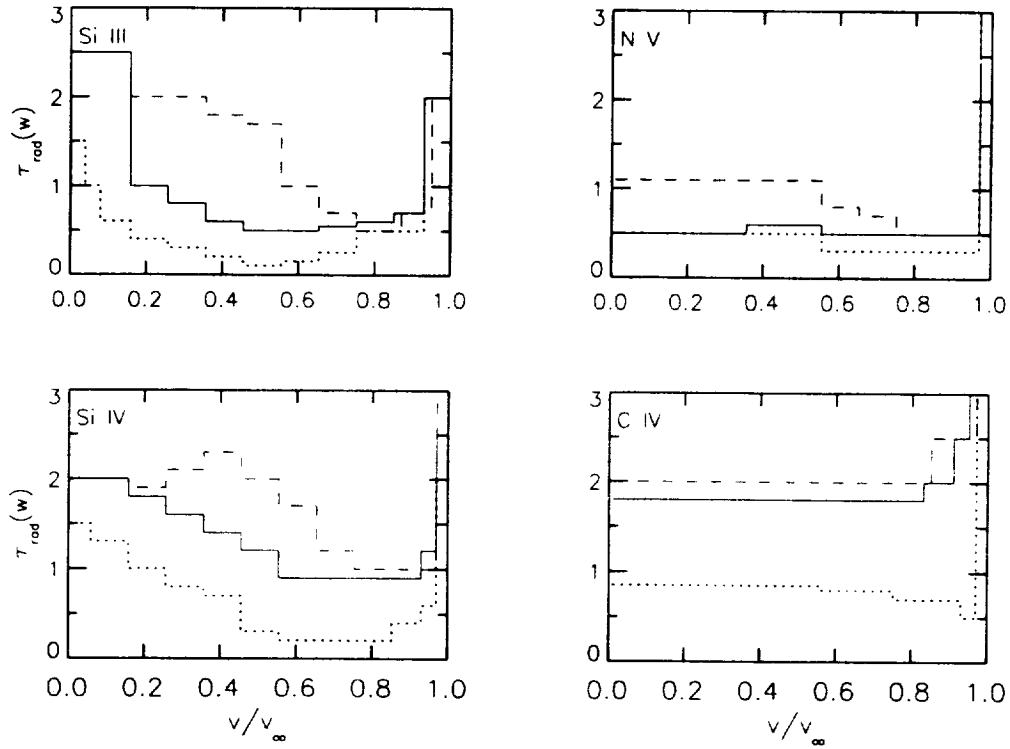

FIG. 7.—Optical depth parameter τ_{rad} vs. normalized velocity for the fits shown in Fig. 5. The dashed, solid, and dotted curves correspond to the maximum, mean and minimum absorption profiles. The τ_{rad} are for Si III λ1206 (*top left*), N V λλ1240 (*top right*), Si IV λλ1400 (*bottom left*), and C IV λλ1550 (*bottom right*).
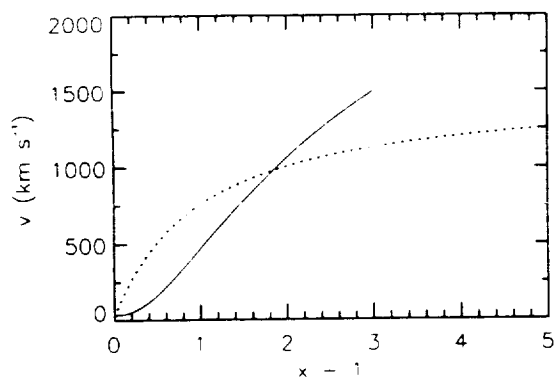
FIG. 8.—Truncated $\beta = 3$ velocity law with a $v_x = 3500$ km s^{-1} (solid curve) compared to the $\beta = 1$, $v_x = 1500$ km s^{-1} velocity law (dotted curve) used to obtain the fits shown in Fig. 5.

(see eq. [1] in Groenewegen & Lamers 1991, hereafter GL) assuming $R = 22 R_\odot$ and cosmic abundances (Anders & Grevesse 1989). The entry for the mean and maximum values for C IV are not as reliable as the others, since this line is approaching saturation in these spectra, although it is clearly unsaturated in the minimum absorption state.

The overall quality of the fits is quite good for Si III and N V, but there is considerable disagreement for in the low-velocity portions of the Si IV and C IV lines. Since we can obtain good fits for the wind lines due to the lowest and highest ions, it seems that the quality of the fits depends only upon the strength of the wind line and not the physics of its formation.

In view of the many degrees of freedom inherent in our fitting procedure, we expect the "tailored" fits to be essentially perfect (see § 5.2). The fact that they are not indicates a breakdown in one of our input functions or perhaps the basic assumptions involved in the SEI theory. Furthermore, the problem encountered in the optically thick ions is not unique to HD 64760, since its profiles are nearly identical to those in HD 100276 and many other B supergiants. The inability of the models to produce enough absorption near $v = 0$ km s^{-1} in strong wind lines has been encountered before. It might be that the synthetic separation between a photosphere and a wind (the "core-halo" model that Sobolev approaches assume) becomes ambiguous when the wind is optically thick (Hamann 1981). It could also be a consequence of spherically symmetric, nonmonotonic wind flows (Puls et al. 1993; Owocki 1995). Another, not wholly independent, solution is also possible, and is considered next.

As can be seen from Si IV and C IV fits in Figure 5, the models produce an excess of scattered light at low velocity. This suggests that the escape probability is too large, or that too large of a volume is contributing to the emission at low velocity. These shortcomings can be investigated within the context of our assumed β velocity law in the following ways. To decrease the volume contributing to the low-velocity emission, we increase the terminal velocity and truncate the opacity at some velocity, $w_e < 1$, which corresponds to 1500 km s^{-1} so that all of the wind absorption and emission occurs between the surface of the star and $r(w_e)$. Such an ionic distribution might occur if the ionization of the wind shifted to higher, unobservable states (perhaps as a result of shocks and X-ray emission) in the outer wind. We decrease the escape probability at low velocity by choosing a velocity law with a large β. In fact, the combination of these two parameters, β and v_∞, can

produce a truncated velocity law that has an acceleration very similar to a $\beta = 1$ law for most velocities, but a much slower acceleration at low velocity. Figure 8 compares such a law ($\beta = 3$, $v_x = 3500$ km s^{-1}, which implies $w_e = 0.43$ and $x = r(w_e)/R = 4$), to the $\beta = 1$, $v_x = 1500$ km s^{-1} law used to produce the fits shown in Figure 5. Figure 9 shows the C IV and N V profiles that result from the truncated velocity law and compares the resulting optical depths to those obtained from the $\beta = 1$ law.

Although the velocity law shown in Figure 8 is unlikely to be appropriate for HD 64760, it suggests that the escape probability of a photon at low velocity is considerably less than that implied by a normal β law. Whether this is due to a shallow velocity gradient at the base of the wind, or to the presence of a nonmonotonic velocity law arising from low-velocity shocks cannot be determined at this stage. Because there is an infinity of velocity laws to choose from there seems to be little point in exploring that parameter space until more theoretical guidance is available. Nevertheless, this solution is interesting and it also shows that the derived optical depths are not too sensitive to the selection of velocity law. It also reminds us that changes in the velocity law can account for considerable line profile variability (see, e.g., Prinja & Howarth 1984).

With the preceding caveats in mind, we now examine some aspects of the fits shown in Figure 5. Of particular interest is the fact that although the absorption varies by a factor of several in the silicon lines, there is little evidence for variability in the observed red emission (see the lower panels in Fig. 2). In contrast, the model fits predict much larger changes in the red emission. These results can be interpreted in terms of structures in wind and used to infer the size and number of such structures.

We begin with the red emission. Because the observed red emission at a fixed velocity emanates from over an entire constant velocity surface, and because the red emission does not vary significantly, the number of structures distributed over a constant velocity surface at any time must be large enough that deviations from the mean do not have a strong impact on the emission. On the other hand, the observed absorption is composed of both light scattered from a constant velocity surface (but the stability of the red emission implies that this contribution must also be fairly stable) and absorption by material along the line of sight to the star (which must account for the variability). The fact that the absorption is highly variable suggests that (1) the responsible structures must be large enough to cover a sizable fraction of the stellar disk in order to have an impact on the observed absorption, and (2) the number of these structures along the line of sight at any given time must be small, so that the motion of one of them into or out of the line of sight can have a strong impact on the observed absorption (see also Prinja & Howarth 1988).

Additional evidence for clumping comes from the way the models tend to underestimate the red emission for the minimum state profiles. Recall that our fitting technique uses the absorption portion of the profile to determine τ_{rad}. So if the wind is clumped and there happens to be far fewer structures than average along the line of sight to the star at the time of the observation being fit, then the fitting procedure will underestimate τ_{rad}. Consequently, if the line is far from saturation, the calculated red emission will be too weak, as observed.

The upper panel of Figure 10 shows the ratios of the optical depths derived from the maximum and minimum absorption states. These ratios can be very large. While the ratio of 17 for
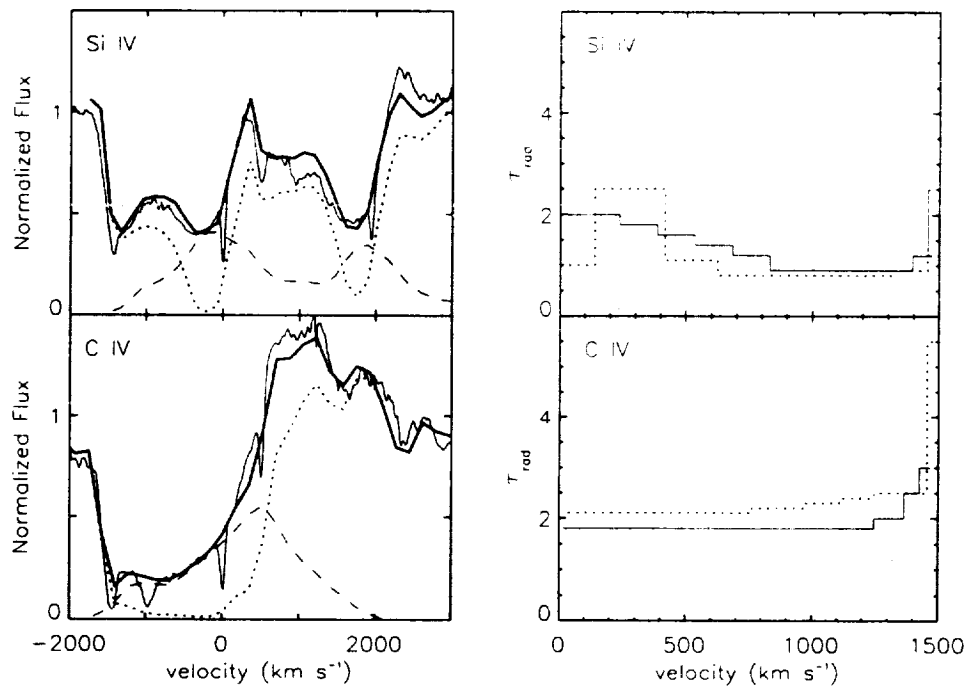
FIG. 9.—Line fits (*left*) and optical depth parameters τ_{rad} (*right*) that result from the velocity law shown in Fig. 8 for the mean profiles of Si IV (*top*) and C IV (*bottom*). The fits show the transmitted and scattered light contributions, and the optical depths show both the τ_{rad} used in the fit shown (*dotted line*) and the one used in the fits shown in Fig. 5 (*solid line*).

Si III near $v/v_\infty = 0.5$ is uncertain because the optical depth of the minimum absorption profile is so small, it is still clear that the column densities must change by factors of 5 to 10 for Si III and IV. Furthermore, it is interesting that these changes are accompanied by more modest changes, ~ 2, in the C IV and

FIG. 10.—Ratios of the τ_{rad} that result from the fits. The top panel shows the ratios of τ_{rad} derived from the minimum and maximum profiles for each ion. This represents the maximum observed variability in the optical depths or, equivalently, column densities. The lower panel shows the ratios of the τ_{rad} resulting from the fits to mean profiles of each ion to that of Si IV.

N V column densities, although this is only a lower limit for C IV, since its maximum absorption profile is becoming saturated and the derived optical depths could easily be increased by 50% without a significant impact on the fit. The fact that the relative changes differ from ion to ion implies that the ionization state of the wind must be time variable, a subject that will be discussed in more detail in § 5.4.

The lower portion of Figure 10 shows the ratios of the optical depths derived from the mean profiles of the different ions to Si IV. The relative abundance of both C IV and N V increase monotonically with velocity, while the relative abundance of Si III initially declines and then begins to increase (a conclusion already reached in § 4.2 for the DACs). These ratios can be converted directly into ratios of local ion fractions, q_i, since

$$\frac{q(X)}{q(\text{Si IV})} = \frac{\tau(X)}{\tau(\text{Si IV})} \frac{(A_E \lambda f)_{\text{Si IV}}}{(A_E \lambda f)_X},\qquad (4)$$

where the A_E are the cosmic abundances of the element relative to hydrogen. At $v = 0.5v_\infty$, one finds (see Table 3) $q(\text{Si III})/q(\text{Si IV}) = 0.15$, $q(\text{N V})/q(\text{Si IV}) = 0.63$, and $q(\text{C IV})/q(\text{Si IV}) = 0.37$.

These ratios can be compared to those listed in Table 2 of GL (also evaluated at $v = 0.5v_\infty$) for the B0 Ia ϵ Ori. This is the only B supergiant in their sample, and the only B supergiant for which both a well-determined mass loss (from radio continuum measurements) and an SEI analysis of its UV lines are available. Because we do not have a well established mass-loss rate for HD 64760, we confine the comparison to the *ionic ratios* given above. The comparison is further limited because we did not analyze C III (we were not confident in assuming a population for its lower, excited state) and GL did not analyze Si III (presumably because it occurs in so few of their program stars). So only two ratios are at our disposal, $q(\text{C IV})/q(\text{Si IV})$
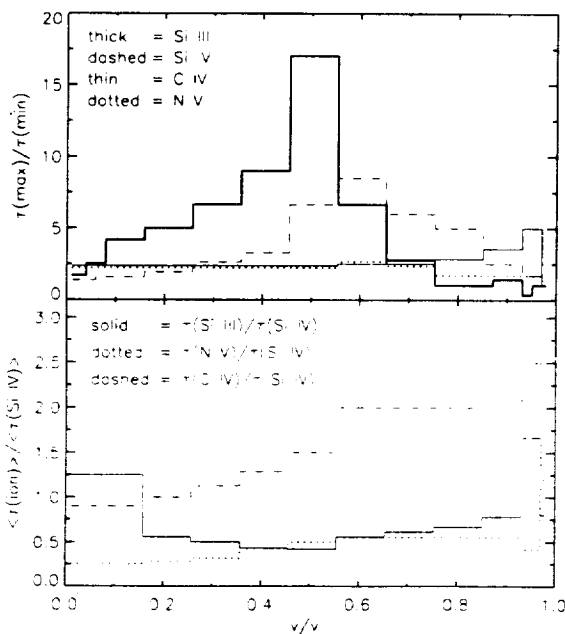
and q(N v)/q(Si iv). The q(C iv)/q(Si iv) ratio is virtually identical for the two stars, 0.40 and 0.36 for ε Ori and HD 64760, respectively. In contrast, their q(N v)/q(Si iv) ratios differ dramatically, 0.066 and 0.62, respectively. While the ion ratios can vary with time (see Fig. 10, § 5.4, and Table 3) a factor of 10 is well beyond the observed variability. In fact, the q(N v)/q(Si iv) ratio in HD 64760 remains effectively unchanged when the wind is in a strong state, *but increases by more than a factor of 3 when the wind is in a weak state.* The high q(N v)/q(Si iv) ratio disagrees with the GL result (their Fig. 3), which shows that q(N v)/q(Si iv) increases with increasing temperature. In fact, the q(N v)/q(Si iv) ratio for HD 64760 is more indicative of late O supergiants like α Cam and ζ Ori. It may be that this difference arises because ε Ori is nitrogen deficient (Walborn 1976), and chemical anomalies can strongly affect the wind line ratios (Walborn & Panek 1985; Massa et al. 1991). However, ζ Ori is also nitrogen deficient and its ion ratios agree with those of the normal supergiant α Cam. It is also possible that the lower ratio in ε Ori is due to its denser wind. Whatever the case, it appears that the behavior of ionic ratios in intermediate luminosity B supergiants is largely unknown, and that considerably more work is needed to put the current results into context.

5.4. Ionization Variability

We now examine how the ionization changes during the different wind events. Ideally, we would " correct " the observed profiles for their scattered light component and derive optical depths directly (see eq.[1]). However, since the quality of the fits is not satisfactory, such an approach has questionable utility. Instead, we proceed as follows. First, the normalized profiles were binned into 100 km s^{-1} bins. Next, we selected a velocity strip in Figure 2 for Si iii λ1206 and N v λ1238 and plotted these against the corresponding Si iv λ1393 points. Finally, the points from the spectra obtained during the time interval of interest are plotted as triangles, and everything else as pluses. As long as the underlying emission does not change, variations in these data are directly related to variations in the column densities.

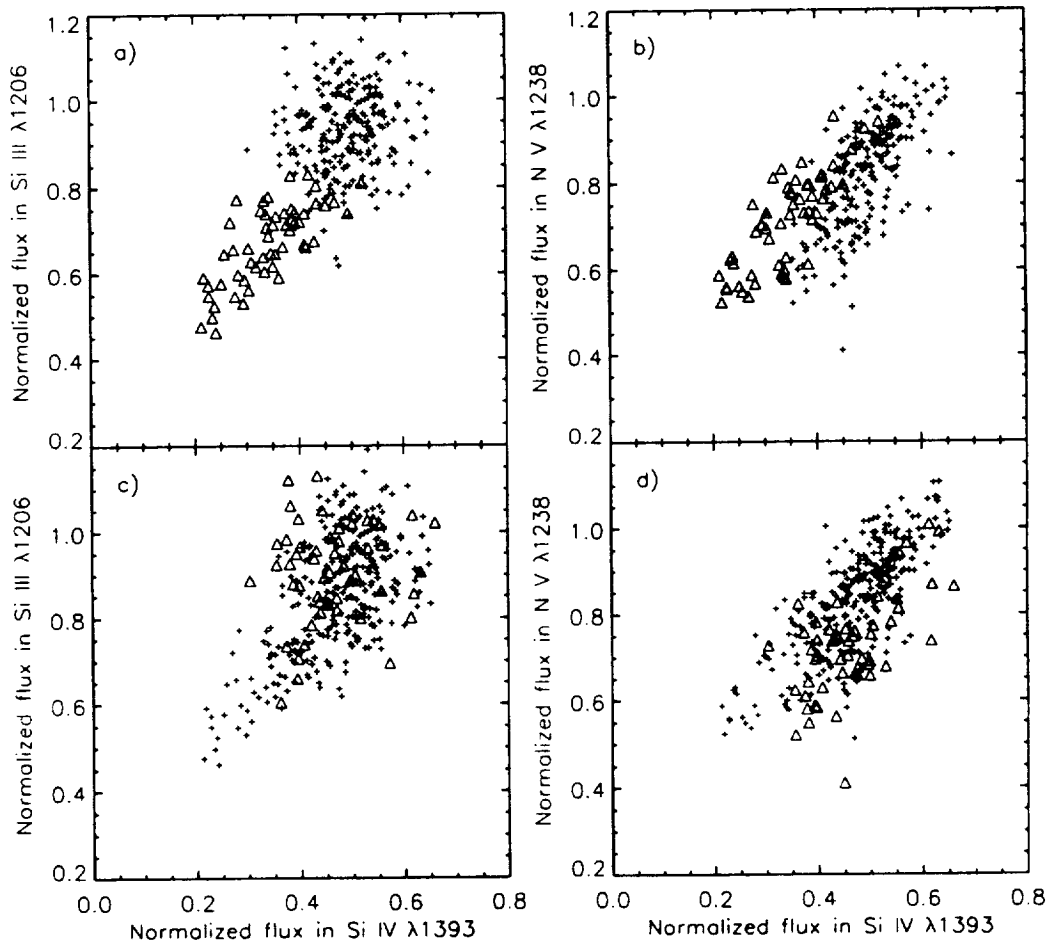Figures 11a and 11b show the results for the *main event*, where the velocity range is from -1000 to -600 km s^{-1} and

FIG. 11.—Scatter plots of the normalized fluxes in N v and Si iii vs. those in Si iv. The points in the upper set are from a [-1000, -600] km s^{-1} strip in Fig. 2 and were binned into 100 km s^{-1} bins. The points from the spectra during main event are plotted as triangles and everything else as pluses. Note that when the flux in Si iv decreases during the event, the N v points follow a different path from those outside the event. For fixed Si iv flux, the N v fluxes are systematically higher, i.e., there is less N v absorption than expected from other times during the series. This shows that the ionization state of the wind decreased during the main event. The lower set of plots are for a [-1100, -600] km s^{-1} strip in Fig. 2 and are similarly binned. The points from the spectra during second strong event (between $\Delta t = 100$ and 200 hr) are plotted as triangles and everything else as pluses. In this case there is some indication that when the flux in Si iv decreases the N v points decrease more strongly than normal relative to Si iv. Consequently, the overall ionization of the wind appears to have *increased* during this event.

the time interval of the event corresponds to the images SWP 47137–47167. We see that when the flux in Si IV decreases during the main event, Si III follows suit (the main event accounts for nearly all of the variability in Si III). However, the N V points during the main event clearly follow a different path from those outside the main event. For fixed Si IV flux, they are *systematically* higher, i.e., there is less N V absorption than would be expected from other times during the series. This demonstrates that the ionization state of the wind *decreased* during the main event.

Figures 11c and 11d show the results for the *second major* event that occurred between $\Delta t = 100$–120 hr and is associated with DACs (4) and (5). We use the velocity range and the time interval corresponding to images SWP 47239–47247. In the scatter plot for the Si III/Si IV ratio, the distribution of the points associated with the event do not differ significantly from others not associated with the main event. On the other hand, it is apparent that there is systematically more N V absorption than normal for fixed Si IV. This demonstrates that the ionization state of the wind *increased* during this event.

Thus, we see that for a given amount of Si IV absorption there was *more* Si III absorption and *less* N V absorption during the main event than during the second major event. Thus, the ionization state of the wind during two major absorption events that occurred during the time series are fundamentally different, perhaps the results of very different physical processes.

5.5. Comparison to Theoretical Models

It is of interest to compare our results with theoretical predictions. We begin by discussing the theoretical mass-loss rate. Adopting this value for $\dot{M}$ enables us to convert our estimates of $\dot{M}q_i$ into actual ionization fractions, q_i, which can then be compared to the ionization structures of different wind models.

We use the radiatively driven stellar wind theory (Kudritzki et al. 1989) with the non-LTE force multiplier parameters discussed by Groenewegen et al. (1989) to determine the mass-loss rate for HD 64760. The accuracy of this approach is assessed by comparing its results to the observed values for ϵ Ori (the only normal BI with a reliable radio mass-loss rate determination). By increasing $L/L_{\odot}$ by just 0.1 dex (well within the observational error) over the value listed by Lamers & Leitherer (1993), we can match the model v_{∞} to the observed value, 1500 km s^{-1}. When this is done, the model predicts a mass-loss rate of $\dot{M} = 1.4 \times 10^{-6}$ $M_{\odot}$, which is somewhat less than the observed value of $4.1 \pm 1.5 \times 10^{-6}$ $M_{\odot}$. Thus, we should keep in mind that, with the terminal velocity fixed, the theoretical model we are using seems to *underestimate* the actual mass-loss rates for stars with physical parameters similar to HD 64760.

For the stellar parameters corresponding to HD 64760 (Table 2), radiative driven stellar wind theory predicts $v_{\infty} = 1900$ km s^{-1} and $\dot{M} = 9.4 \times 10^{-8}$ $M_{\odot}$. However, these are mean B0.5 Ib values, and it is possible to obtain a $v_{\infty} \sim 1500$ km s^{-1} while remaining within the B0.5 Ib bin. This can be accomplished by either increasing the luminosity by 0.2 dex, or decreasing the mass to 16 $M_{\odot}$. In the first case the mass loss increases by a factor of 2, and in the latter it increases by 20%. So the terminal velocity can be brought into accord with theory, but we must be willing to accept a mass-loss rate of more than 10^{-7} $M_{\odot}$ yr^{-1} (recall that this theoretical prediction is probably an underestimate). In this case the q_i must be $\leq 1\%$ for the higher stages of ionization.

If $q_i \leq 1\%$ for Si IV, C IV and N V and somewhat less for Si III, these values and their ionic ratios are very different from Drew's (1989) predictions for a radiative stellar wind in thermal equilibrium (GL reach a similar conclusion for the O stars). At the effective temperature of a B0.5 Ib, one would expect nearly all of the silicon in Si IV and only trace amounts of N V. The observed ratios may imply, as Drew suggests, the presence of distributed X-rays.

Although no wind model incorporating the effects of distributed X-rays has been constructed with parameters corresponding to HD 64760, we can use the available models to speculate on the effects X-rays might have on the ionization structure of its wind. For dense winds (e.g., ζ Pup; MacFarlane et al. 1993; Pauldrach et al. 1994) the X-rays only perturb the ionization state of the wind slightly. On the other hand, they dominate the ionization structure in the rarefied winds of main-sequence B stars (MacFarlane, Cohen, & Wang 1994). In the latter models, the amount of Si IV present is always very low relative to C IV or N V, and whenever $q(N\ V)/q(C\ IV) \sim 1$, the absolute values of $q(N\ V)$ and $q(C\ IV)$ are ≥ 0.1, nearly 10 times that inferred from the *predicted* mass-loss rate.

Thus, it is possible that the observed ionic ratios represent an intermediate state between a wind dominated by X-rays and the ab initio model. However, in either case, it seems that the ion fractions are too low if the predicted $\dot{M}$ is correct.

Another way to produce the observed ionization ratios is, as Drew (1989) suggests, to attribute much of the Si IV to density enhancements, in the form of "clumps" or "structures," in a wind whose ionization structure is otherwise dominated by the distributed X-rays. This presents the notion of a two-component wind consisting of a highly ionized ambient wind interspersed with denser, less highly ionized structures.

Certain aspects of our results support this picture. First, in spite of the N V and Si IV wind lines having similar optical depths, the variability in the Si IV column density is *much larger* than in N V (see Table 3 and Fig. 10). This leads us to associate the Si IV with the less highly ionized structures (although much of the N V must also be identified with these structures since the amounts of the two species present are generally correlated, see Fig. 11). Second, when the line-of-sight wind optical depth is a minimum (see Table 3), the $q(N\ V)/q(Si\ IV)$ ratio is a maximum, suggesting that the ionization state of the "ambient" wind is higher than when the line of sight to the star intercepts strong optical depth enhancements, with their smaller values of $q(N\ V)/q(Si\ IV)$. Unfortunately, the ionization shifts during the *second major event* are contrary to the expectations of this model. Thus, the situation may be more complex than a simple two-phase wind whose individual components have uniform properties.

Regardless of how the wind is structured, *neither* the X-ray dominated *or* the ab initio models predict $q(N\ V)/q(Si\ IV) \sim 1$ *unless* $q(N\ V)$ *and* $q(Si\ IV)$ are both ≥ 0.1. But this result conflicts with the theoretical mass loss. Thus, the only way to reconcile the ionization ratios is to concede that the mass-loss rate is 10 times less than predicted. However, this is at odds with recent findings for O star winds, which suggest that the theory systematically *underestimates* the actual mass-loss rates (Lamers & Leitherer 1993).

It is unfortunate that bright B0–1 Ib stars have not been observed at X-ray wavelengths. It would also be of interest to obtain radio observations of some of these stars in order to obtain estimates of their total mass-loss rates and help determine whether the observed ions actually have such small values of q_i.

6. SUMMARY

Since this is the first intensive study of the time-dependent behavior of the stellar wind of an intermediate luminosity B supergiant, it is impossible to determine which aspects of the observed variability are unique to HD 64760 and which are common to all such stars. Although the spectrum of HD 64760 is, in all respects, that of a normal B0.5 Ib it would be premature to draw wide ranging conclusions from this one star until we are more certain how it fits into the general context of intermediate luminosity B supergiants. Nevertheless, the activity in this star has provided several intriguing results. Among these are the following:

Continuous wind activity.—At no time during our 6 day run was the wind in steady state for more than a few hr. During this time, the equivalent widths of the wind absorption between -2000–0 km s^{-1} of the stronger wind lines varied by as much as 50%, with the implied column densities changing by more than a factor of 5 at some wavelengths.

Low-velocity wind variability.—There is evidence in the C II and Al III resonance lines and the Si III triplets that excess material is moving outward from $v \simeq 0$ km s^{-1} at the beginning of a prolonged period of enhanced absorption (the main event). There is also a hint of possible infall in Al III just prior to the main event.

A photospheric connection.—The "photospheric" Si III $\lambda\lambda 1300$ triplets shifted by ~ -20 km s^{-1}, and strengthen by more the 25% at the beginning of the main event, and even the C III $\lambda 1247$ singlet shifted by more than -10 km s^{-1} and strengthened noticeably at this time. These observations provide the strongest evidence yet for a connection between photospheric and wind activity. It is also possible that some of the activity seen at low velocity in the stronger wind lines is actually due to variability in the underlying "photospheric components" of the lines—as in the Si III triplets.

Long temporal coherence.—The main event lasts for an entire day, and (with a few exceptions) the major changes that occurred during the time series progressed rather smoothly in time. This kind of extremely long temporal coherence is difficult to explain in terms of a stochastic process such as shocks, and even challenges the timescales available to nonradial pulsations. It suggests that at least the variability associated with this episode is rooted in the photosphere, possibly modulated by the rotation of the star. However, to determine whether there is a causal link to the rotation of the star, or whether rotation is simply a relevant timescale requires observations spanning several rotation periods.

Large-scale spatial coherence.—The weakening period appears to provide an example of large-scale spatial coherence, with a simultaneous weakening in several lines across a wide range in velocities. This occurrence is most naturally interpreted as a spatially coherent structure moving out of the line of sight. There is no indication of a shift in the ionization of the wind during the weakening period.

Ionization variability.—We were also able to detect shifts in the ionization of the wind. The shifts that occurred during the two major wind events (i.e., increases in the absorption) are distinctly different. During the main event the mean level of ionization in the wind decreased (suggesting a global density enhancement), while during the second event it appears that the ionization of the wind increased.

In addition to these results, modeling of the wind lines also provided some unique information about the state of the wind in this particular star and perhaps about radiatively driven winds in general:

Constraints on the wind structure.—There is no strong evidence for red emission variability, and this contradicts the model fits to the minimum and maximum profiles that predict noticeable differences. This result implies that the absorption variability is from relatively small ($\ll 4\pi$ sr) structures that happen to be in the line of sight to the stellar disk. Furthermore, the strong variability in the absorption indicates that the number of such structures on that portion of a constant velocity surface that occults the stellar disk at a particular time must be quite small. In contrast, the stability of the red emission (which originates over an entire constant velocity surface) implies that the number of structures throughout the wind at a given time must be large enough that their mean number does not vary significantly.

Inferences about the low-velocity escape probability.—The fits suggest that the escape probability at low velocity is overestimated by a normal $\beta \sim 1$ velocity law. This could be due to the presence of low-velocity shocks deep in the wind (a non-monotonic velocity law), a shallow velocity gradient at low velocity, or a broader problem with the theory.

Wind ionization structure.—Because of the presence of several unsaturated lines, we were able to derive more reliable estimates for the ionization structure of a radiatively driven stellar wind than previously possible. The ion fraction ratio, $q(\text{N v})/q(\text{Si iv})$, is much greater in HD 64760 than in ϵ Ori, contradicting trends inferred from O star data. This large ratio is also inconsistent with thermal equilibrium wind models, and almost certainly results from X-rays distributed throughout the wind. The large $q(\text{N v})/q(\text{Si iv})$ ratio can be explained in terms of a distributed X-ray wind model, but only if we accept that the theoretical mass-loss rate is too large by a factor of 10 or more. Thus, it is impossible to reconcile the observed ionization ratios and the predicted mass-loss rate within the framework of the available models.

Clearly, considerably more research on BIs needs to be done. Hopefully, this paper has demonstrated the utility of these objects for addressing several of the outstanding questions concerning the physical processes operating in stellar wind flows.

REFERENCES

Anders, E., & Grevesse, N. 1989, Geochim. Cosmochim. Acta, 53, 197
Balona, L. A. 1975, MNRAS, 78, 51
Boggess, A., et al. 1978a, Nature, 275, 372
———. 1978b, Nature, 275, 377
Bohlin, R. C. 1975, ApJ, 200, 402
Drew, J. E. 1989, ApJS, 71, 267
Giddings, J. R., & Rees, P. C. T. 1989, SERC Starlink User Note 37 (London: SERC)
Groenewegen, M. A. T., & Lamers, H. J. G. L. M. 1991, A&A, 243, 429 (GL)
Groenewegen, M. A. T., Lamers, H. J. G. L. M., & Pauldrach, A. W. A. 1989, A&A, 221, 78
Hamann, W. R. 1981, A&A, 93, 353
Henrichs, H. F. 1988 in O Stars and Wolf-Rayet Stars, ed. P. S. Conti & A. B. Underhill (NASA SP-497), 199
Henrichs, H. F., Kaper, L., & Zwarthoed, G. A. A. 1988, in A Decade of UV Astronomy with the IUE Satellite (ESA SP-281, vol. 2), 145
Hoffleit, D., & Jaschek, C. 1982, The Bright Star Catalogue (New Haven: Yale Univ. Press)
Howarth, I. D. 1992, in ASP Conf. Ser. 22, Nonisotropic and Variable Outflows from Stars, ed. L. Drissen, C. Leitherer, & A. Nota (San Francisco: ASP), 155
Howarth, I. D., & Prinja, R. K. 1989, ApJS, 69, 527
Howarth, I. D., & Reid, A. H. N. 1993, A&A, 279, 148
Humphreys, R. M., & McElroy, D. B. 1984, ApJ, 284, 565
Kaper, L. 1993, Ph.D. thesis, Univ. Amsterdam
Kudritzki, R. P. Pauldrach, A., Puls, J., & Abbott, D. C. 1989, A&A, 219, 205
Lamers, H. J. G. L. M., Cerruti-Sola, M., & Perinotto, M. 1987, ApJ, 314, 726
Lamers, H. J. G. L. M., Gathier, R., & Snow, T. P. 1982, ApJ, 258, 186
Lamers, H. J. G. L. M., & Leitherer, C. 1993, ApJ, 412, 771
Lucy L. B. ApJ, 1971 163, 95

MacFarlane, J. J., Cohen, D. H., & Wang, P. 1994, ApJ, 437, 351
MacFarlane, J. J., Waldron, W. L., Corcoran, M. F., Wolff, M. J., Wang, P., & Cassinelli, J. P. 1993, ApJ, 419, 813
Massa, D. 1989, A&A, 224, 131
———. 1995, ApJ, 438, 376
Massa, D., Altner, B., Wynne, D., & Lamers, H. J. G. L. M. 1991, A&A, 242, 188
Massa, D., Shore, S. N., & Wynne, D. 1992, A&A, 264, 169
Moffat, A. F. J., Owocki, S. P., Fullerton, A. W., & St-Louis, N., eds. 1995, Instability and Variability in Hot-Star Winds (Dordrecht: Kluwer)
Moffat, A. F. J., & Robert, C. 1994, ApJ, 421, 310
Owocki, S. P. 1995, in Instability and Variability in Hot-Star Winds, ed. A. F. J. Moffat, S. P. Owocki, A. W. Fullerton, & N. St-Louis (Dordrecht: Kluwer), 3
Pauldrach, A. W. A., Kudritzki, R. P., Puls, J., Butler, K., & Hunsinger, J. 1994, A&A, 283, 525
Prinja, R. K. 1988, MNRAS, 231, 21P
———. 1992, in Asp Conf. Ser. 22, Nonisotropic and Variable Outflows from Stars, ed. L. Drissen, C. Leitherer, & A. Nota (San Francisco: ASP), 167
Prinja, R. K., & Howarth, I. D. 1984, A&A, 133, 110
———. 1986, ApJS, 61, 357
———. 1988, MNRAS, 233, 123
Puls, J., Owocki, S. P., & Fullerton, A. W. 1993, A&A, 279, 457
Schaller, G., Schaerer, D., Meynet, G., & Maeder, A. 1992, A&AS, 96, 269
Snow, T. P. 1977, ApJ, 217, 760
Walborn, N. R. 1976, ApJ, 205, 419
Walborn, N. R., & Panek, R. J. 1985, ApJ, 291, 806
Weinstein, D., & Carini, M. 1992, IUE NASA Newsletter, 49, 5
York, D. G., Vidal-Madjar, A., Laurent, C., & Bonnet, R. 1977, ApJ, 213, L61